Cell Reports

Article

A dynamic bifurcation mechanism explains cortex-wide neural correlates of conscious access

Graphical abstract

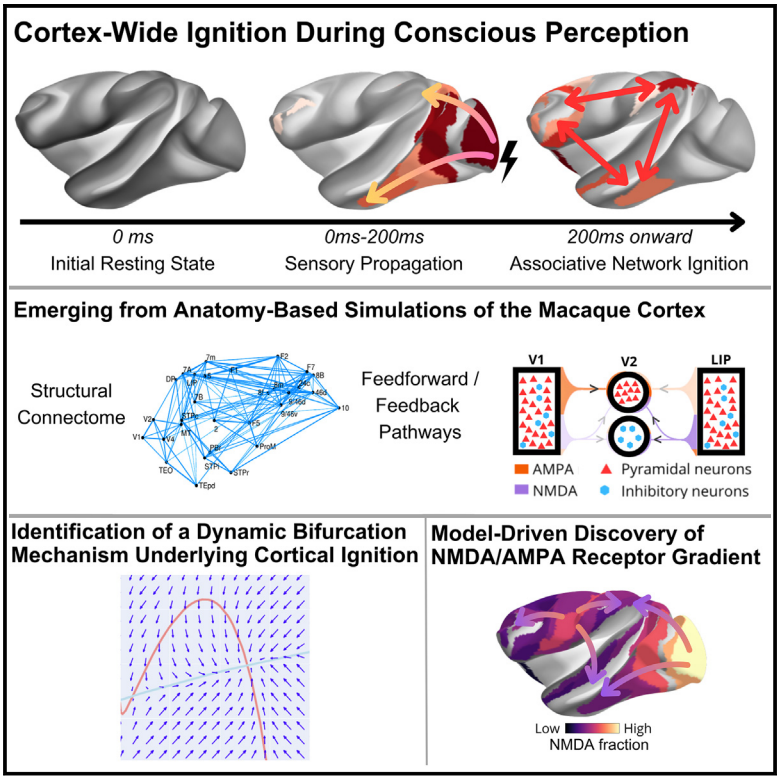

Highlights

- A dynamic bifurcation mechanism reproduces "ignition-like" all-or-none cortical activity
- The connectome defines a unified, all-or-none network in association cortex
- A hierarchical AMPA/NMDA receptor gradient supports these ignition dynamics in the cortex
- Cortex-wide *in vitro* autoradiography confirms the predicted AMPA/NMDA gradient

Authors

Ulysse Klatzmann, Sean Froudist-Walsh, Daniel P. Bliss, ..., Claire Sergent, Stanislas Dehaene, Xiao-Jing Wang

Correspondence

xjwang@nyu.edu

In brief

Klatzmann et al. identify a network-based bifurcation mechanism underlying conscious access. Using a mesoscale biophysical model, they reveal all-or-none dynamics emerging from connectome structural organization via an NMDA/AMPA receptor gradient. They validated this prediction using cortex-wide *in vitro* autoradiography. These findings provide insights into neural dynamics supporting conscious access.

Klatzmann et al., 2025, Cell Reports *44*, 115372
March 25, 2025
https://doi.org/10.1016/j.celrep.2025.115372

CellPress

Cell Reports

CellPress
OPEN ACCESS

Article

A dynamic bifurcation mechanism explains cortex-wide neural correlates of conscious access

Ulysse Klatzmann,[1,2,3,11] Sean Froudist-Walsh,[3,11] Daniel P. Bliss,[1] Panagiota Theodoni,[1,4] Jorge Mejías,[5] Meiqi Niu,[6] Lucija Rapan,[6] Nicola Palomero-Gallagher,[6,7] Claire Sergent,[2,8] Stanislas Dehaene,[9,10] and Xiao-Jing Wang[1,12,*]

[1]Center for Neural Science, New York University, New York, NY 10003, USA
[2]Université de Paris Cité, INCC UMR 8002, 75006 Paris, France
[3]Bristol Computational Neuroscience Unit, School of Engineering Mathematics and Technology, University of Bristol, Bristol BS8 1UB, UK
[4]Center for Mind, Brain, and Consciousness, Department of Philosophy, New York University, New York City NY 10003, USA
[5]Swammerdam Institute for Life Sciences, University of Amsterdam, Amsterdam, the Netherlands
[6]Institute of Neuroscience and Medicine (INM-1), Research Center Jülich, Jülich, Germany
[7]C. and O. Vogt Institute for Brain Research, Medical Faculty, University Hospital Düsseldorf, Heinrich Heine University, 40225 Düsseldorf, Germany
[8]CNRS, INCC UMR 8002, Paris, France
[9]Collège de France, 11 Place Marcelin Berthelot, 75005 Paris, France
[10]Cognitive Neuroimaging Unit, CEA, INSERM, Université Paris-Sud, Université Paris-Saclay, NeuroSpin Center, 91191 Gif/Yvette, France
[11]These authors contributed equally
[12]Lead contact
*Correspondence: xjwang@nyu.edu
https://doi.org/10.1016/j.celrep.2025.115372

SUMMARY

Conscious access is suggested to involve "ignition," an all-or-none activation across cortical areas. To elucidate this phenomenon, we carry out computer simulations of a detection task using a mesoscale connectome-based model for the multiregional macaque cortex. The model uncovers a dynamic bifurcation mechanism that gives rise to ignition in a network of associative regions. A hierarchical N-methyl-D-aspartate (NMDA)/α-amino-3-hydroxy-5-methyl-4-isoxazolepropionic acid (AMPA) receptor gradient plays a critical role: fast AMPA receptors drive feedforward signal propagation, while slow NMDA receptors in feedback pathways shape and sustain the ignited network. Intriguingly, the model suggests higher NMDA-to-AMPA receptor ratios in sensory areas compared to association areas, a prediction supported by *in vitro* autoradiography data. Furthermore, the model accounts for diverse behavioral and physiological phenomena linked to consciousness. This work sheds light on how receptor gradients along the cortical hierarchy enable distributed cognitive functions and provides a biologically constrained computational framework for investigating the neurophysiological basis of conscious access.

INTRODUCTION

Among the huge flow of information received by our sensory organs, only a fraction of it is consciously perceived.[1] The network, cellular, and synaptic mechanisms of conscious perception are hotly debated and largely unresolved.[2–8] In many experiments that probe the access of stimuli to consciousness, subjects (human or non-human) are presented with faint stimuli and asked to report if they detect them. Neural activity in early sensory areas grows approximately linearly with stimulus strength, regardless of whether the stimulus is detected.[9–14] However, when a stimulus is consciously detected, activity commonly emerges across the frontal and parietal cortex in an all-or-none fashion and is sustained for a few hundred milliseconds[9–19] in stable[20] or reliable dynamic trajectories.[21,22] This widely distributed, sudden, and sustained activity has been termed "ignition."[2,23]

Several prominent theories of consciousness propose a central role of recurrent synaptic interactions between excitatory neurons.[3,23] However, the timescale of excitatory synaptic interactions differs drastically depending on the type of postsynaptic glutamatergic receptors. The most widely expressed of these are α-amino-3-hydroxy-5-methyl-4-isoxazolepropionic acid (AMPA) and N-methyl-D-aspartate (NMDA) receptors. Experimental and theoretical work on working memory has emphasized the importance of AMPA receptors for rapid responses in the early sensory cortex and of NMDA receptors for sustaining activity in the prefrontal cortex.[24–26] However, studies of conscious perception have hypothesized a critical role of NMDA receptors at long-distance feedback connections (which has been partially supported experimentally,[27]). This may imply a large proportion of NMDA receptors in major targets of feedback connections, such as in the early sensory cortex, seemingly in contrast to work from the working memory literature. It is unclear whether these two positions are compatible or whether the ignition phenomenon is critically dependent on the synapses at which AMPA and NMDA receptors are expressed.

Small-scale simulations of brain areas organized in perfect hierarchy with NMDA-mediated feedback connections have reproduced the late sustained activity.[12,23,28] Though critical for building intuitions, by abstracting away from anatomy, small-scale simulations limit the anatomical specificity of predictions and may overlook major problems that the brain must overcome to enable ignition, such as propagation of information through a strongly recurrent large-scale system.[29] Large-scale modeling studies based on real cortical connectivity data have investigated the dynamic propagation of stimulus information into the frontoparietal network but have not captured the late sustained activity that is seen experimentally.[29–31] A realistic large-scale model of the ignition phenomenon should create testable, anatomically precise predictions for theories of consciousness, reproduce key physiological findings from detection experiments across the sensory and association cortex and behavior, and offer a platform for future simulations of other experimental paradigms.

In this study, we develop a mesoscale connectome-based dynamic model of the macaque cortex with realistic biophysical constraints and assess its behavior during a stimulus detection task, similar to that used experimentally. Second, we examine whether the parameter regime necessary for realistic model behavior is consistent with receptor distributions in the macaque cortex. Our model reproduces multiple aspects of monkey behavior and physiology, including aspects that have evaded previous models, such as strong propagation of activity through the connectome to the prefrontal cortex, bifurcation dynamics, and sustained activity across a distributed subsets of frontoparietal regions. Furthermore, we demonstrate that sufficiently strong stimulus propagation and ignition require NMDA/AMPA distributions across the cortex that closely match those measured experimentally. Therefore, our findings shed light on the synaptic and systems-level mechanisms underlying ignition and reconcile seemingly contradictory anatomical, physiological, and modeling results.

RESULTS

A large-scale dynamic model of the macaque cortex with NMDA, AMPA, and GABA receptors

We built a large-scale model of the macaque cortex containing 40 different interacting cortical areas. Each cortical area contains a local circuit with two populations of excitatory neurons and one population of inhibitory neurons.[32,33] Excitatory connections are mediated by both NMDA and AMPA receptors, and inhibitory connections are mediated by $GABA_A$ receptors. Cortical areas differ in the strength of excitatory input (due to differences in the expression of dendritic spines[34]) and are connected according to weighted and directed inter-areal connections, measured by retrograde tract tracing[35] with data from 40 interconnected areas.[36]

Stimulus detection is accompanied by widespread ignition of activity throughout the frontoparietal network

We simulated a stimulus detection task by injecting differing, small amounts of external current to the primary visual cortex (V1) for 50 ms (Figure 1A). In the V1, average activity over trials increased approximately linearly with stimulus intensity before returning to baseline a few milliseconds after the stimulus was removed (Figure 1B). In contrast, on many trials, activity in areas throughout the prefrontal and parietal cortices reached a high activity state at around 200 ms (Figures 1B and 1C; Data S1). This activity remained stable until the end of the trial or until the vigilance signal was removed. This pattern of prefrontal and early visual activity closely matches the dynamics of neural activity in the monkey prefrontal cortex during a similar task.[12] We therefore interpret trials with late, sustained activity in area 9/46d of the dorsolateral prefrontal cortex as corresponding to detection of the stimulus[12] (i.e., hit trials) and trials without such activity as miss trials.

Activity in the frontoparietal network, but not sensory areas, distinguishes hit from miss trials

Average activity over trials in sensory areas was very similar for hit (stimulus present and detected) and miss (stimulus present but not detected) trials (Figure 1B). Therefore, regardless of whether the stimulus was detected, neural activity in sensory areas reliably tracked the objective stimulus strength. In contrast, while hit trials engaged strong, sustained activity throughout frontal and parietal cortices, miss trials led to either a transient increase in activity, which returned to baseline, or no increase in activity (Figure 1B). The sensory and prefrontal findings closely correspond to experimental findings from visual and somatosensory detection experiments,[9,11,12] validating the model. Beyond the primary sensory cortex and dorsolateral prefrontal cortex (dlPFC), our model therefore predicts that, when a stimulus is detected, late stimulus-related activity should be detectable throughout a distributed prefrontal and posterior parietal cortical network (Figure 1C).

The probability of detecting a stimulus increases nonlinearly with stimulus intensity

Due to the stochastic single-trial behavior, it is possible to analyze how the proportion of hit trials varies with stimulus intensity. Note that late activity always proceeded to either a high or low activity state, as seen in monkey and human experiments.[12,37] The proportion of hits increased with the stimulus intensity, with a sigmoidal curve accurately fitting the data (Figure 2), as observed frequently in monkeys and humans.[10,12,13]

Transition from early unimodal to late bimodal neural activity in stimulus detection

During stimulus detection tasks, early ($\langle 200ms \rangle$) cortical activity increases with increasing stimulus strength, irrespective of whether the stimulus is later detected or missed. When plotted across trials, this early activity creates a unimodal distribution[37] and likely corresponds to pre-conscious processing.[38] After ~250 ms, activity either increases to a high-activity state or returns to a low-activity state,[37] thus creating a bimodal cross-trial distribution, with only the high activity state corresponding to the conscious detection of the stimulus. Thus, Sergent and colleagues suggest that trial activity proceeds from a dynamic sequence of early states to one of two possible late activity states (for prior evidence; see, e.g., Sergent and Dehaene[39]).

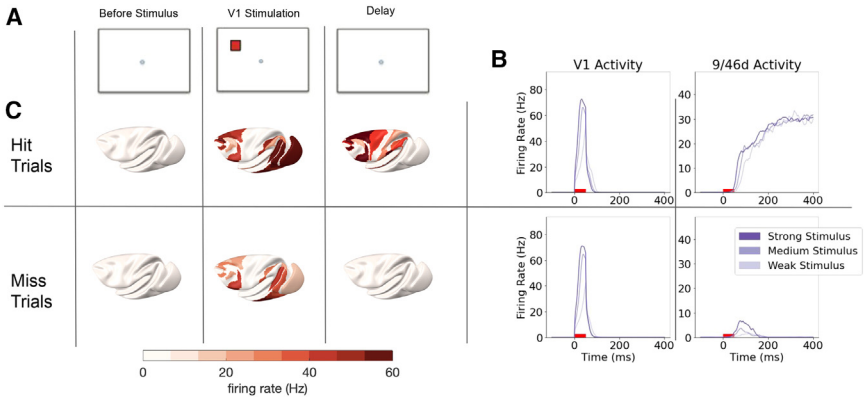

Figure 1. Stimulus detection is accompanied by widespread ignition of activity throughout the frontoparietal network

(A) Task structure. A near-threshold stimulus is presented to the excitatory population in area V1 for 50 ms.

(B) Top: averaged activity over trials in V1 (primary visual cortex) and area 9/46d (prefrontal cortex) during hit trials for differing levels of stimulus intensity (200, 250, and 300 pA for weak, medium, and strong stimulus strengths). V1 activity rapidly increases to a peak that differs according to stimulus intensity before falling back to baseline. 9/46d activity, in contrast, reaches a high sustained activity state after about 200 ms, which does not depend on stimulus intensity. Bottom: averaged activity over trials in V1 and area 9/46d during miss trials for differing levels of stimulus intensity. V1 activity is very similar to that on hit trials. 9/46d activity differs drastically, with a smaller peak of activity followed by a return to a low firing baseline state.

(C) Firing rates across the cortex during example hit (top) and miss (bottom) trials. Hit trials are accompanied by sustained activity throughout much of prefrontal and posterior parietal cortex, which is absent on miss trials.

In (B) and (C), stimulus intensity and network parameters are completely matched between hit and miss trials, which differ only in the random noise.

This may hint at a bifurcation (i.e., a change in the number or stability of internal states) occurring over time.

Following the methods of Sergent et al., we analyzed model activity at each time point across several trials and examined whether activity across trials was best described by a null distribution (neural activity independent of the stimulus), unimodal distribution, or bimodal distribution. Shortly following the stimulus, activity was best described by a unimodal distribution. After approximately 100 ms, the data were best described by a bimodal distribution (Figure 3A), matching experimental observations in humans detecting auditory stimuli.[37] In our model, we detect a shift to a bimodal cross-trial distribution after about 100 ms, with late activity reaching its peak in prefrontal cortex after 200 ms (Figure S1). This broadly matches the timing of stimulus-induced prefrontal activity observed in monkey experiments, which is observable from $\sim 60\,ms$ following stimulus onset and peaks after $\sim 150 - 200\,ms$[12,40,41]. Therefore, our connectome-based dynamic model accounts for the temporal progression of activity states observed in the brain during stimulus detection tasks.

A dynamic-to-sustained progression of activity states associated with ignition

Previous studies of conscious perception have reported that neural dynamics evolve from a dynamic to a relatively stable activity pattern.[20,42] We aimed to decode the trial outcome (hit/miss) from activity at each time point for a fixed stimulus near the threshold of detection using the temporal generalization method.[43,17] We defined trial outcome based on activity in area 9/46d and predicted this outcome using activity in all other cortical areas (therefore avoiding circularity). We observed a dynamic succession of patterns coding for stimulus visibility in the early trial stages, with reasonably high classification accuracy remaining close to the diagonal (Figure 3B, bottom left box). In the

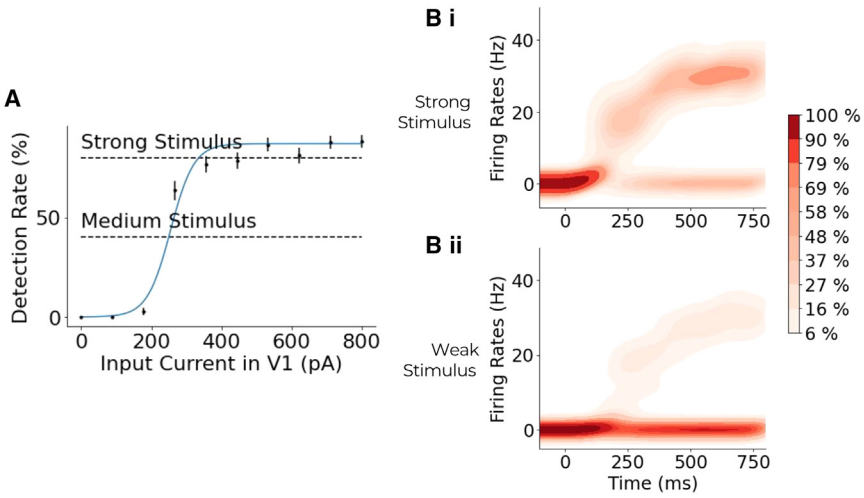

Figure 2. A sigmoidal relationship between stimulus intensity and detection probability

(A) The rate at which the large-scale cortical model detects the stimulus (engages sustained activity over 15 Hz in area 9/46d) increases non-linearly with the stimulus intensity (input current in V1).

(B) The distributions of firing rates across trials for area 9/46d in the large-scale model for strong (about 80% detection rate) and weak (about 20% detection rate) stimuli. The outcome of individual trials is stochastic, depending on the noise in the system, but the system always ends in either a high-activity state, corresponding to stimulus detection, or a low-activity state, corresponding to a miss. A higher percentage of trials with a strong stimulus end in the high-activity state compared to trials with a weak stimulus (as seen by the darker red in the high-activity branch after 200 ms). The stimulus is presented at 0 ms for 50 ms.

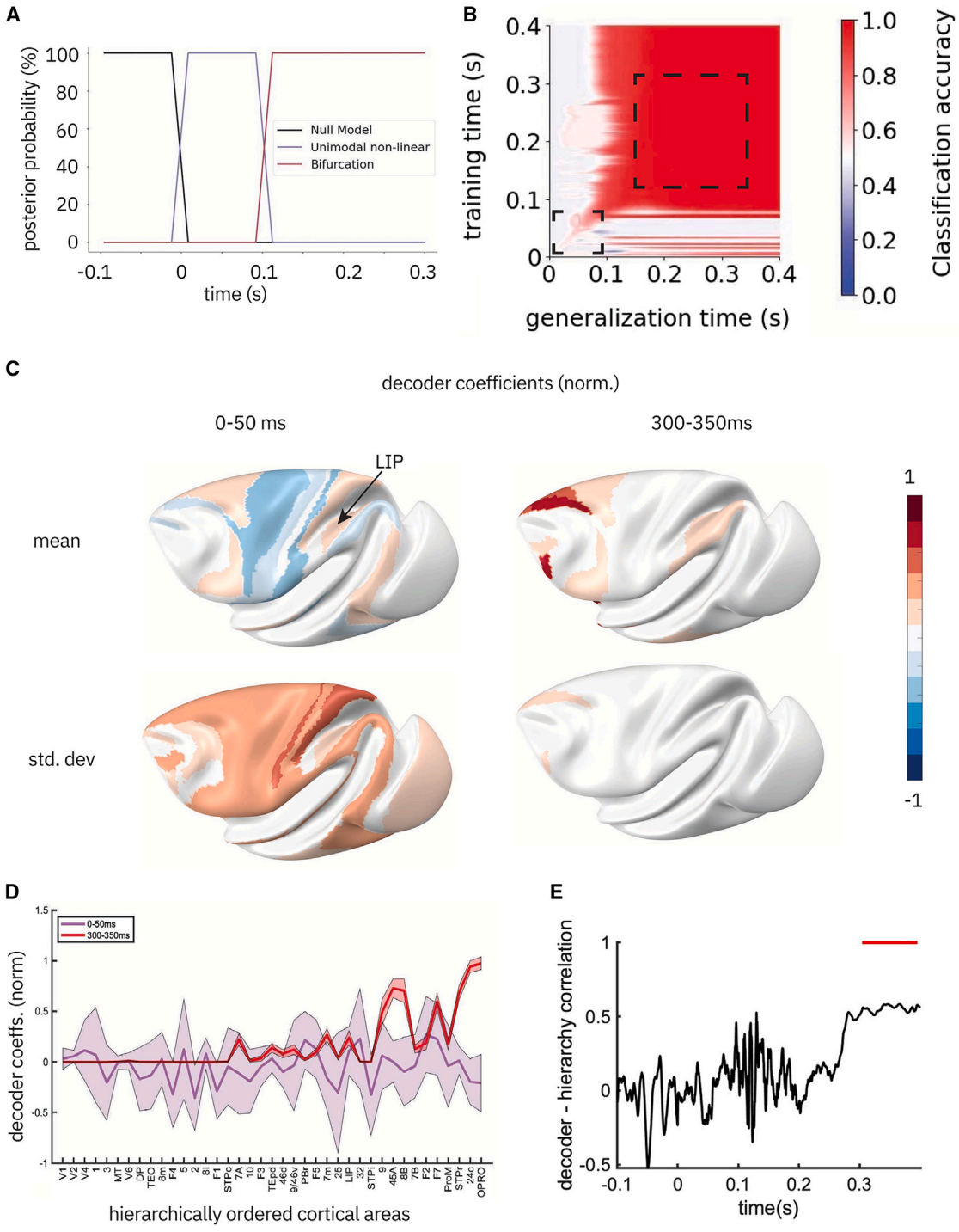

Figure 3. A dynamic-to-sustained progression of activity states associated with ignition

(A) Across-trial statistics of neural activity for different stimulus strengths were used to classify model neural activity as belonging to null (black), unimodal (purple), or bimodal (red) distributions at each time point. Activity progresses from a null distribution to unimodal and finally bimodal across-trial activity distributions, indicative of a bifurcation.

(B) Temporal generalization matrix. For stimuli at the detection threshold (about 50% detection rate), a classifier trained to decode trial outcome (hit/miss) from the activity pattern at each time point in a training dataset is used to predict outcome based on the activity at each trial time point in held-out data. A diagonal pattern (e.g., in the bottom left dashed box) indicates a quickly changing dynamic code. A square pattern (e.g., in the top right dashed box) indicates a stable code.

(C) Cortical surface representation of the mean and SD of the normalized decoder coefficients for early (0–50 ms) and late (300–350 ms) periods of the trial.

(legend continued on next page)

later trial period, we observed a stable pattern of high decoding accuracy, with the decoders trained between $\sim 100 - 400\,ms$ generalizing to all other time points within that range (Figure 3B, top right box). Classifiers trained on some early time points had below-chance accuracy at decoding later time points (blue patches in Figure 3B). This indicates that early activity patterns are effectively reversed later in the trial. Similar results have been reported in the human experimental literature.[37,44] Our model suggests that the below-chance generalization from early to late time points may be due to higher associative areas sending net inhibitory feedback to areas that are lower in the visual hierarchy. Put another way, the stable, ignited activity pattern can lead to a reversal of the activity patterns that occur during stimulus propagation.

Decoding coefficients were highly variable over the first 50 ms (Figures 3C, left, and 3D) before settling on a pattern (300–350 ms) of high coefficients throughout a distributed network of frontal, parietal, and some temporal regions. The standard deviation remains high only in regions of the frontal cortex to which activity propagates last. The coefficients of the late decoder are higher in areas that are high in the cortical hierarchy (Figure 3D). A significant and stable correlation between decoder coefficients and the cortical hierarchy emerges late in the trial, after about 300 ms (Figure 3E). This demonstrates how a stable code throughout the frontoparietal cortex can coexist with a dynamic activity in some areas of the cortex (Figure 3C). This prediction can be tested experimentally.

A dynamic bifurcation mechanism for ignition underlies stimulus detection

The previous analyses hinted at the possibility of a bifurcation occurring during stimulus detection. To better understand the dynamics determining whether individual trials would result in a hit or a miss, we built a simplified local model with a single area made of a single excitatory and a single inhibitory population (Figure 4A). The equations are the same as in the full model, only the connectivity is different. Additionally, we focused on excitation mediated by the NMDA receptors. This reduces the system to two dynamic variables corresponding to the synaptic variables S_{NMDA} and S_{GABA}. This simplification enables us to analyze the dynamics of individual areas by looking at their phase portraits.[45]

We analyze the dynamics for hit and miss trials (Figure 4B; Data S1). The system initially has two stable steady states (attractors) corresponding to low- and high-activity states (excitation close to 0 and excitation close to 0.5) and an unstable steady state (repeller, at about excitation 0.2). Before the stimulus, the system begins at the low steady state. The stimulus to the excitatory neural population shifts the excitation nullcline up, reducing the number of nullcline crossings from three to one. The single remaining crossing represents a stable steady state, and activity is attracted toward this high-activity state during the stimulus. Due to noise, the speed at which the activity increases toward the nullcline crossing differs. When the stimulus is removed (“early post stimulus”), the nullclines rapidly shift back to their original position. As the unstable steady state (the middle nullcline crossing) repels activity away from itself, this effectively acts as a threshold. When the stimulus is removed, any activity to the left of the unstable steady state is attracted back to the low-activity steady state, resulting in a miss, while any activity to the right is attracted toward the high-activity steady state, leading to a hit (Figure 4C). A stronger stimulus will lead to a larger shift in the excitatory nullcline, which increases the probability of trajectories reaching the basin of attraction of the high-activity state (i.e., a hit). Therefore, the dynamic activity patterns of hits and misses can result from transient bifurcations induced by the external stimulus and noise.

Fast propagation of stimulus information to the prefrontal cortex depends on feedforward excitation mediated by AMPA receptors

The transient sensory activity and persistent prefrontal activity seen above and experimentally[12,11] suggest that, unusually for a recurrent network, different parts of the cortex may act in different dynamic regimes (i.e., monostable vs. bistable). Although the connectivity and spine count in our model are taken from anatomical data, the cell-type targets of the inter-areal connections (excitatory or inhibitory) and which glutamatergic receptors mediate these connections (AMPA or NMDA) are unknown. We therefore performed a parameter search to uncover the combinations of cell-type targets and glutamatergic receptors that can reproduce such dynamics.

We allowed the parameters for feedforward and feedback components of pathways to vary independently. We used the fraction of supragranular labeled neurons (SLN) as a validated marker of the degree of “feedforwardness” of a pathway[46] but did not explicitly include layers in the model. Here, we refer to the sum of axons from any area to another as a “pathway,” which is made up of a combination of SLN (i.e., pure feedforward) and 1-SLN (i.e., pure feedback) components. For example, the pathway from V1 to V2, which is a classic feedforward pathway, has an SLN of 0.72 (from previous data[36]).

We found three distinct regimes of model behavior in response to a brief, strong, 50-ms visual stimulus: transient activity that returns to baseline (No Bistability), sustained activity across all cortical areas (Whole-Cortex Bistability), and sustained activity only in association areas of the cortex (Subnetwork Bistability) (Figures 5A and 5B). The reference parameter set used in all figures of the study (unless specified otherwise) was taken from this Subnetwork Bistability regime.

We observed that, to obtain subnetwork bistability dynamics, feedforward components of pathways in the model should target mainly excitatory cells, principally via AMPA receptors (Figures 5A and 5B. In contrast, the feedback components of pathways should target both excitatory and inhibitory cells, with a greater contribution of NMDA receptors.

(D) Mean (±SD) of the normalized decoder coefficients for early (0–50 ms) and late (300–350 ms) periods of the trial as a function of the hierarchical position of each cortical area.

(E) Correlation (Pearson’s r) between the decoder coefficients at each time point and the cortical hierarchy. The red bar shows the time range with a statistically significant correlation.

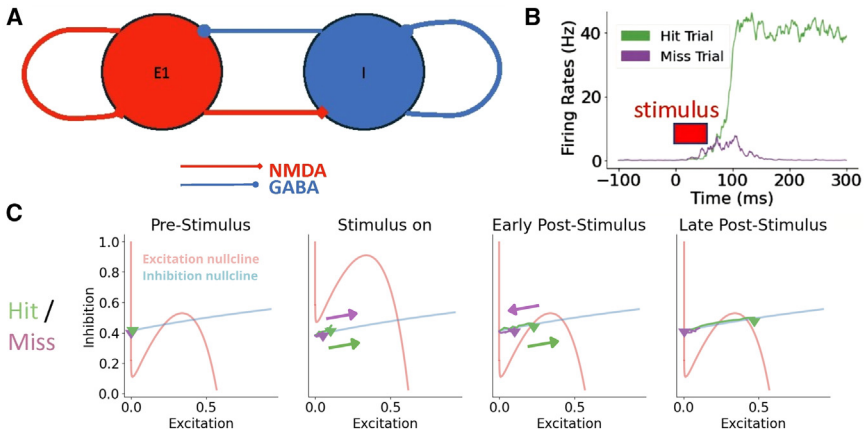

Figure 4. A dynamic bifurcation mechanism for ignition underlies stimulus detection

(A) Simplified circuit for analysis of dynamics, containing a single excitatory and a single inhibitory population, interacting via NMDA and GABA receptors.

(B) Firing rates from area 9/46d in the large-scale system on individual hit (green) and miss (purple) trials.

(C) Phase portrait of the simplified network at different trial stages. Example dynamics for individual hit and miss trials are shown in green and purple, respectively. The stimulus causes the excitation nullcline (red) to move up, reducing the number of crossings with the inhibition nullcline (blue). Removal of the stimulus moves the nullclines back to the original positions. In the hit trial, by the time the stimulus has been removed, activity has reached the basin of attraction of the high-activity steady state and progresses toward it (right nullcline crossing). In the miss trial, activity remains in the basin of attraction of the low-activity steady state (left nullcline crossing) and returns toward it after removal of the stimulus.

We next performed a separate parameter search to identify parameter sets that could replicate realistic propagation times (Figure S1). Notably, a strongly overlapping set of parameters was required to replicate rapid ignition within the realistic 130- to 200-ms range.[10,12,40] Specifically, we found that feedforward components targeting excitatory cells via AMPA receptors and feedback components targeting inhibitory and excitatory cells with a greater NMDA-dependent contribution allow the feedforward excitation to transiently "escape" the inhibition and successfully propagate stimulus-related activity along the cortical hierarchy. Therefore, the pattern of feedforward AMPA-mediated excitation and mixed feedback (NMDA + AMPA) is required to replicate the spatiotemporal activity of sensory and associative areas during stimulus detection.

We next focused on one classic feedforward pathway (V1 → V2), two feedback pathways (V2 → V1 and LIP → V2), and one lateral pathway (LIP → 9/46d; Figure 5C) from the cortex-wide model (reference parameter set). The NMDA fraction (expressed as $\frac{G_N\tau_N}{G_N\tau_N+G_A\tau_A}$, where $\tau_{N/A}$ is the receptor time constant) was highest in inter-areal feedback pathways, followed by inter-areal lateral pathways, and lowest in feedforward pathways. However, in all of these pathways, there remains a significant AMPA contribution. We then cut all the inter-areal connections but LIP to V2 and injected a strong and brief (10-ms) current in LIP. Despite LIP to V2 being a feedback connection and having one of the largest NMDA contributions in the network, the peak of the resulting inter-areal AMPA current is over five times greater than the peak of the NMDA current (Figure 5D). Despite the dominance of AMPA at inter-areal connections overall, in our model, it is an important observation that the NMDA coupling is stronger in feedback and lateral pathways than feedforward pathways, a prediction that remains to be measured experimentally.

Ignition depends on NMDA receptor activation in local excitatory connections

Does ignition also depend on the receptors that mediate local intra-areal excitation? We adjusted the model so that the NMDA fraction of local excitatory connections varied. For a very low NMDA fraction, we see sustained activity in the frontoparietal network but at unrealistically high firing rates (mean frontoparietal delay activity = 173 Hz for local NMDA fraction = 0.2; Figure 5E). Only models with a relatively high fraction of local excitatory connections mediated by NMDA receptors showed sub-network bistability and sustained activity in the frontoparietal network at a reasonable firing rate (mean frontoparietal delay activity = 40 Hz for local NMDA fraction = 0.8, Figure 5E). However, if local connections were completely mediated by NMDA receptors, then bistability was lost. This suggests that a contribution of AMPA-mediated excitation is helpful to engage NMDA-mediated excitation and sustained activity. Therefore, our model suggests that NMDA receptors at local excitatory connections are crucial for ignition of cortical activity in response to a stimulus, in support of the previous theoretical[25] and experimental[26] findings.

The NMDA/AMPA ratio decreases along the cortical hierarchy

We calculated the NMDA fraction (as a fraction of NMDA- and AMPA receptor-mediated excitation) for each area in the model (Subnetwork Bistability parameter set). In the model, we observed a strong decrease in the NMDA fraction along a 40-area cortical hierarchy (Figure 6A, $r = -0.71, p = 3 \times 10^{-7}$, hierarchy data from[36]). This decreasing NMDA fraction gradient is not seen in the networks that are incapable of producing realistic ignition dynamics (Whole-Cortex Bistability, No Bistability parameter sets) (Figure S2). This leads to a testable nontrivial prediction: the cortical hierarchy, if capable of subnetwork bistability and rapid ignition, should have a decreasing NMDA fraction gradient.

We tested this prediction by analyzing *in vitro* receptor autoradiography data from 109 regions of the macaque cortex.[47–51] By dividing the receptor density by the neuron density in each area,[36,51,52] we were able to estimate the NMDA and AMPA density per neuron in each area (Figure 6B). We found that both the NMDA ($r = 0.70, p = 1 \times 10^{-5}$) and the AMPA ($r = 0.80, p = 3 \times 10^{-8}$) receptor densities per neuron

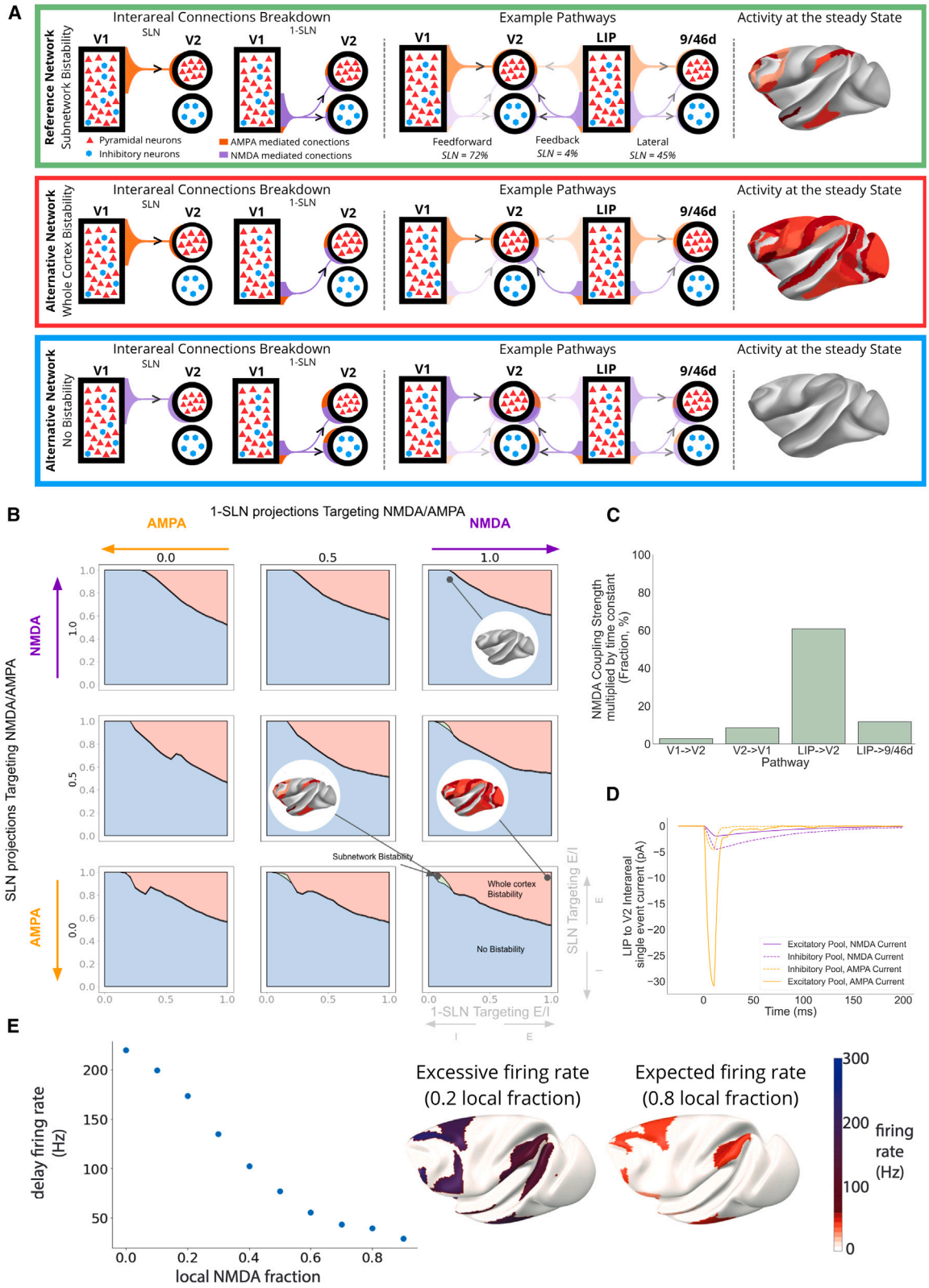

(legend on next page)

increased along the cortical hierarchy (Figure 6C). We defined the "NMDA fraction" in each area as the NMDA receptor density divided by the sum of the NMDA and AMPA receptor densities. Despite the increases in both NMDA and AMPA densities along the hierarchy, there was a strong negative correlation between the NMDA fraction from the experimental data and the cortical hierarchy (Figures 6D and 6E, $r = -0.81, p = 2 \times 10^{-8}$), confirming our model prediction.

The decreasing NMDA/AMPA gradient supports ignition

We then adjusted the model parameters to match the experimentally observed NMDA and AMPA receptor densities and spine counts.[53] In Figure 5, we show how the NMDA fraction at feedforward and feedback connections critically determines ignition time. We therefore maintained the NMDA fraction at feedforward and feedback connections from the reference model (an assumption on proximity of this aspect of the reference model to biology). However, we allowed the NMDA fraction at local connections to vary across areas so that the overall NMDA fraction of each area in the model closely matched that observed in the receptor autoradiography data. Without changing any other parameters, we observed that this receptor data-based simulation displayed subnetwork bistability dynamics (Figure 6F). Therefore, our previous result is robust to a more biologically constrained parameter set. This supports our prediction that a decrease in the NMDA fraction along the hierarchy may have evolved to enable the dynamic inter-areal interactions required to support ignition-like dynamics.

DISCUSSION

We developed a large-scale model of the monkey cortex to simulate a detection task, building on the previously proposed Global Neuronal Workspace (GNW) architecture[23,28] by integrating newly available weighted and directed cortical connectivity[35,36,46,54,55] and receptor data.[47–51] The model replicates key spatial and temporal features of neural activity observed during conscious perception. Specifically, we found that frontoparietal ignition depends on feedforward excitation mediated by AMPA receptors, while NMDA receptors are crucial for sustaining activity. The model also predicts a decreasing NMDA/AMPA ratio along the cortical hierarchy in the macaque, which we confirmed using receptor autoradiography data. This decreasing ratio facilitates rapid information propagation and ignition of distributed networks during conscious perception, aligning with patterns observed in both human and nonhuman animals.

A dynamic-to-stable transition of cortical activity during conscious perception

The whole-cortex model allows us to track neural activity with millisecond-level temporal resolution and area-level spatial resolution. We inject the stimulus into V1, where it propagates through the visual streams to areas such as V2, V4, and LIP. In the early sensory regions, activity is transient, returning to baseline a few dozen milliseconds after stimulus removal, with stronger stimuli eliciting higher activation. Although activity in these regions is slightly higher during hit trials, it alone cannot reliably predict conscious perception.

A second phase begins around 200 ms, marked by a sudden ignition of a large network of associative frontoparietal regions. These regions exhibit a late activation, with hit trials showing firing rates of approximately 40 Hz and miss trials dropping to near baseline ($\lesssim$5 Hz). Thus, when viewed across hit and miss trials, late activity in these areas resembles a bimodal distribution, as seen experimentally.[37] Notably, while the model was explicitly fitted to ensure bistable activity in area 9/46d, the biological constraints of the connectome resulted in approximately 17 areas displaying bifurcation dynamics, aligning well with the GNW predictions.[23,28] Following this burst, activity in these regions stabilizes for several hundred milliseconds, resembling the sustained activity observed in conscious working memory,[33,36] suggesting a shared mechanism.

However, despite the late sustained activity, stimulus representations were not stable throughout the trial. Temporal decoding analysis reveals that the representation of the stimulus evolves as information flows through the cortex. During the early phase, representations are dynamic and change rapidly, but they stabilize in the later phase, consistent with findings from experimental studies.[17]

No-report paradigms experiments suggest that the strong prefrontal activity initially linked to conscious perception might

Figure 5. Rapid ignition depends on AMPA-dominated feedforward connections and balanced NMDA/AMPA-mediated excitation at feedback connections

(A) Top: representative connections of a parameter set resulting in subnetwork bistability. Top left: schematic of projections from V1 to V2. The target (pyramidal vs. inhibitory neurons) and glutamatergic receptor (AMPA vs. NMDA) mediating the connections depend on the SLN. Top center: three representative pathways, corresponding approximately to feedforward (V1 to V2, SLN = 0.72), feedback (LIP to V2, SLN = 0.04), and lateral pathways (LIP to 9/46d, SLN = 0.45). The opacity reflects the strength of each type of connection within the pathway. Top right: the steady-state firing rate across the cortex following a strong stimulus for this parameter set. Center: same as top for a parameter set resulting in whole-cortex bistability. Bottom: same as top for a parameter set resulting in no bistability.

(B) Four-parameter search over glutamatergic receptors (AMPA/NMDA) and cellular targeting (excitatory/inhibitory) of inter-areal connections (performed separately for SLN and 1-SLN, corresponding approximately to feedforward and feedback components of each pathway). The models exhibit three distinct dynamic behaviors—subnetwork bistability (green), whole cortex bistability (red), and no bistability (blue)—with the former most consistent with empirical observations. Example parameter sets from (A) are mapped onto this space for reference.

(C) Pathway-specific NMDA contribution. Inter-areal NMDA coupling strength multiplied by the time constant, calculated as $G_N\tau_N/(G_N\tau_N + G_A\tau_A)$, of the reference network for a feedforward pathway (V1 → V2), two feedback pathways (LIP → V2 and V2 → V1), and a lateral pathway (LIP → 9/46d).

(D) Inter-areal synaptic currents from LIP to V2 when all other inter-areal connections are removed and a brief stimulus is applied to LIP.

(E) Left: average firing rate in areas showing delay activity for models with different local NMDA fractions. Right: delay period activity across the cortex for models with different local NMDA fractions (top: local NMDA fraction = 0.2; bottom: local NMDA fraction = 0.8). Only the models with a relatively high fraction of local excitation mediated by NMDA receptors can reproduce realistic frontoparietal activity levels.

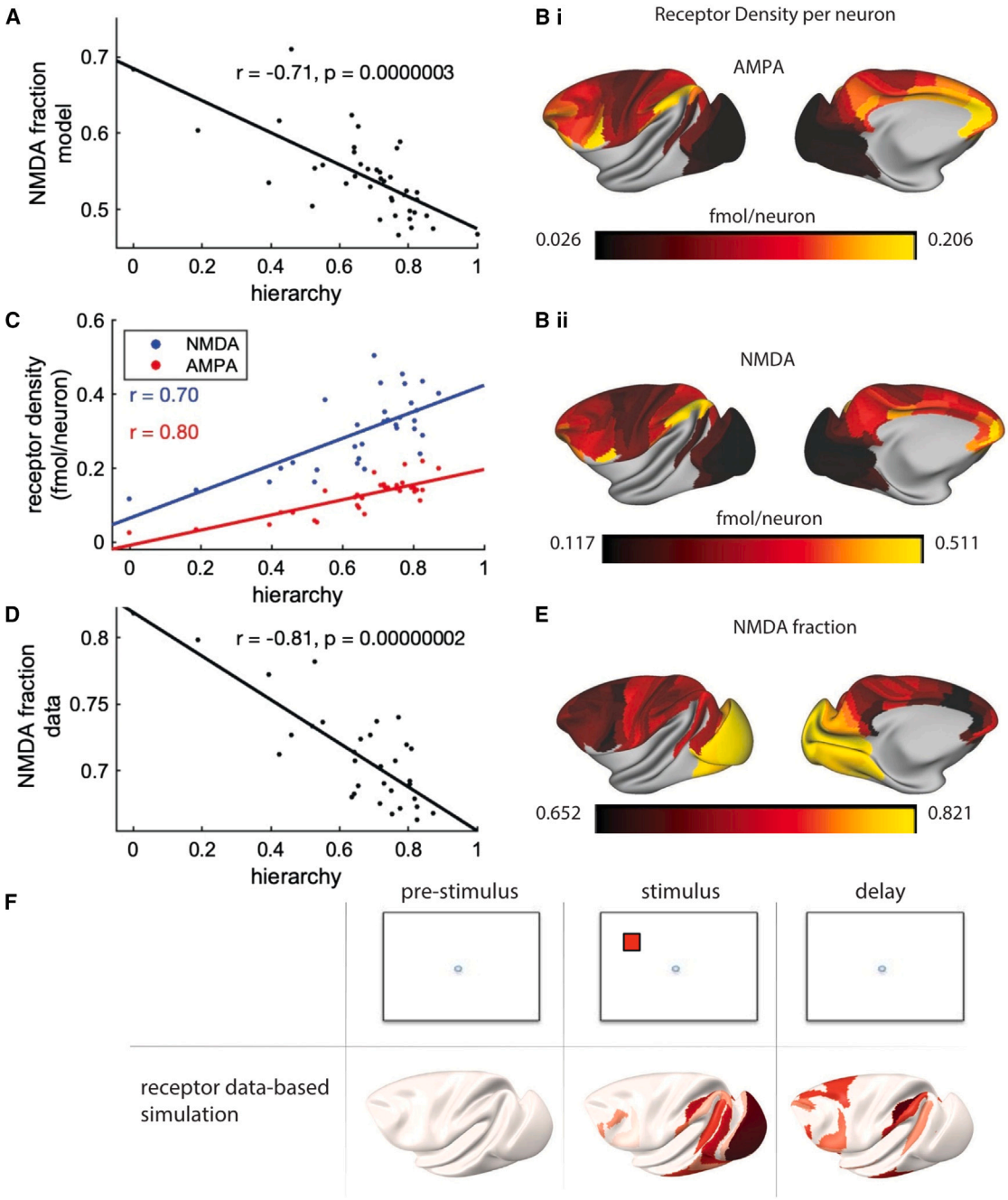

Figure 6. The NMDA/AMPA ratio decreases along the cortical hierarchy and supports ignition

(A) The fraction of excitatory inputs via NMDA receptors (compared to total NMDA+AMPA inputs) in the model decreases along the hierarchy.

(B) The density of (i) AMPA and (ii) NMDA receptors across 109 regions of the macaque cortex. Receptor density was measured using *in vitro* receptor autoradiography and divided by the neuron density data from Collins et al.[52]

(C) AMPA and NMDA densities per neuron both increase along the cortical hierarchy.

(D and E) The fraction of NMDA receptors (compared to total NMDA+AMPA receptors) in the macaque receptor autoradiography data decreases along the hierarchy.

(F) The model was adjusted to match the receptor densities observed in the autoradiography data. The receptor data-based model shows ignition of fronto-parietal activity in response to a visual stimulus.

instead reflect motor preparation.[37,56–61] However, recent findings reveal that, even without explicit report, a network of frontoparietal regions continues to exhibit bifurcation dynamics, whereas activity in premotor regions disappears.[37] Future large-scale models incorporating motor preparation tasks could help disentangle these processes.

Network, cellular, and synaptic mechanisms of conscious access

Using dynamic systems theory, we identified a mechanism that could explain the ignition of a network of neurons: the dynamic bifurcation. In this framework, the system has two stable attractors—a resting state and an excited state. When a stimulus is presented, the nullclines shift, leaving only the excited attractor. The system transitions toward this attractor, increasing neural activity. Upon stimulus removal, the system either reaches the basin of attraction of the excited state, resulting in rapid ignition, or remains in the basin of the resting state, returning to baseline. Importantly, the stronger the stimulus, the greater the nullcline shift, making it more likely for the system to settle in the excited basin of attraction. This analytical dynamic closely aligns with the behavior observed in the network of associative regions during our simulations. These results position dynamic bifurcation as a compelling candidate for explaining the ignition phenomenon underlying conscious access.

At the macroscale level, conscious perception in our model is defined by a sudden surge of activity spreading nearly simultaneously across a frontoparietal network. This network-wide activity enables a coherent representation of the stimulus to be maintained across the cortex while exerting top-down modulation that inhibits lower sensory regions.[33,62–64] This strong, sudden frontoparietal activity corresponds closely to the ignition phenomenon predicted by the global workspace theory.[23,28] Although sustained activity in the early sensory cortex has been observed in some studies,[65–67] its consistency remains unclear, with many studies reporting minimal or no sustained neural activity.[12,68] This aligns with our simulations, where early sensory regions do not exhibit bimodal activity during the late phase of trials and are not essential for maintaining the conscious percept in working memory. A plausible explanation for the variability in early sensory activity is that many tasks do not require representations of fine stimulus features, making sustained activity in the early sensory cortex unnecessary.

Our model identifies NMDA receptors as crucial for the ignition phenomenon, linking this role to broader experimental findings. NMDA spikes, localized within the dendrites of pyramidal cells, enhance the likelihood of plateau-like calcium spikes that propagate to the soma.[7] This dendrite-soma coupling diminishes under anesthesia.[69] Furthermore, activation of the apical dendrites of subcortically projecting layer 5 pyramidal cells in the somatosensory cortex is strongly associated with stimulus detection,[70] potentially by engaging subcortical vigilance signals.[71–73] Together with these recent cellular discoveries, our findings highlight NMDA receptors' pivotal role in cortical dynamics and provide key insights into the synaptic mechanisms underlying conscious processing.

Asymmetric feedforward and feedback excitation via AMPA and NMDA receptors reconciles contrasting anatomical and physiological findings

Many physiological and computational studies suggest that early visual areas rely more on local AMPA receptors for rapid stimulus encoding,[24] while local NMDA receptors are crucial in associative areas for working memory,[25,26] pointing to an increasing NMDA/AMPA ratio along the cortical hierarchy. However, human anatomical studies have revealed the opposite pattern, with a decreasing NMDA/AMPA ratio as one moves up the hierarchy.[74,75]

Our model, which incorporates both local and inter-areal projections, provides a new perspective on these seemingly contradictory findings. To replicate the global dynamics observed in experiments, the model required both NMDA and AMPA receptors at local connections, and an increased presence of AMPA receptors in feedforward inter-areal pathways, facilitating rapid and robust signal propagation. Conversely, NMDA receptors were relatively more abundant in feedback pathways, although their absolute proportion remained small and targeted more inhibitory populations, enabling modulation of lower areas and preserving the integrity of the information represented in the associative network. With lower hierarchical regions being heavily targeted by NMDA-mediated feedback pathways, we observe a decreasing NMDA/AMPA gradient along the hierarchy. This model prediction was tested *in vivo* using autoradiography, and the receptor fractions were incorporated into the model, reproducing experimentally observed neural dynamics. These results underscore the robustness and plausibility of the model. This predicts that NMDA-mediated excitation increases progressively from inter-areal feedforward connections to feedback connections and finally to local recurrent connections. To our knowledge, this has not yet been explicitly measured and remains a testable prediction of the model.

Many studies have reported NMDA/AMPA ratios at excitatory synapses,[76–85] although they typically do not distinguish between inter-areal feedforward, feedback, and local recurrent connections. These studies consistently show contributions from both NMDA- and AMPA-mediated excitatory transmission, with the ratio varying based on experimental conditions and neither receptor type completely dominating at higher membrane potentials. Limited indirect evidence[27] suggests that AMPA receptors drive feedforward visual information propagation, while NMDA receptors support slower responses in recurrent and feedback connections. Similarly, in our model, excitatory transmission is never purely mediated by NMDA or AMPA receptors, reflecting the balance observed experimentally. Although few studies have examined the net effects of feedforward and feedback connections,[62–64] one recent study found that feedback connections exert a slight net inhibitory effect on their targets,[64] contrasting with the strong net excitatory effects of feedforward connections. This finding aligns with our model's results, which highlight the same distinction, and should be further tested experimentally, including through ultrastructural analyses.

Integration of the model in the consciousness literature

The present work proposes a neural mechanism for conscious access, the cognitive function that lets a stimulus enter in the

current stream of consciousness [1] and makes it reportable, verbally or non-verbally.[2,5] The other cognitive functions associated with consciousness, such as metacognition, self-awareness, or any form of attention, are not addressed. Two major current theories of consciousness, among many,[86] are GNW theory[23] and integrated information theory (IIT).[4] Our model fits in the GNW literature, as it possesses the major characteristics of the global workspace; namely, independent sensory modules competing to pass their information to a widely distributed set of areas that broadcast the information to vast parts of the cortex. It differs from previous computational models of the GNW in that it is built explicitly on mesoscopic connectome data and therefore makes predictions for cortex-wide neural activity during detection tasks as well as receptor distributions across the cortex. The associative areas responsible for ignition in the model, heterogeneously connected by the fraction of labeled neurons matrix, resemble the core of the mesoscopic connectome[54] as well as the specialized majority network taken as an example of a high Phi complex,[87] as stated by the IIT for the origin of phenomenological consciousness.[4] However the location of the cortical areas, predominantly in the frontal and parietal cortices, seems to fit more precisely with GNW theory than IIT, which attributes conscious perception primarily to a posterior cortical "hot zone."[88] Further anatomically constrained large-scale modeling, or analysis of our model, could make explicit the areas of agreement and disagreement between GNW and IIT. Future work addressing aspects of metacognition, attention, predictive processing, emotional awareness, conscious volition, or conscious thinking could aim to further bridge GNW with other prominent theories of consciousness[6,89–93] and provide much-needed testable predictions about behavior and neural dynamics to distinguish between such theories.[94–96]

Our current model was specifically designed to replicate brain activity triggered by a brief, faint stimulus. This approach is often used in the study of neural correlates of conscious perception.[12,37] Despite this, there is a host of other experimental paradigms where the identical stimulus can alternatively be perceived or missed. These paradigms include masking,[97,98] attentional blink,[99,100] and binocular rivalry.[101,102] Recent advancements in no-report binocular rivalry experiments have unveiled precise patterns of activity in the temporal and prefrontal cortices. These studies allow for effective decodability of the conscious percept in both the infero-temporal cortex[102] and the lateral prefrontal cortex.[101] Future work could investigate the network activity during such experiments, replicating these precise electrophysiological results and enabling predictions at the whole-cortex scale.

According to the global workspace rheory, this sudden ignition of neural activity is the neural correlate of the broadcasting of information across the brain, which corresponds to the moment a stimulus reaches conscious awareness (conscious access). By proposing a specific neurobiological implementation of this hypothesis, our model makes predictions at the theoretical and mechanistic levels. The theoretical prediction is that a dynamic bifurcation, spatially distributed across the brain, underlies the ignition phenomenon. The mechanistic prediction is that, to support the ignition phenomenon at realistic timescales, NMDA-mediated excitation must be (1) low at inter-areal feedforward synapses, (2) relatively higher at inter-areal feedback synapses, and (3) relatively high at local recurrent synapses. Global workspace theory can be invalidated by demonstrating that ignition does not correspond to the access of a stimulus to conscious awareness (e.g., conscious access without ignition or vice versa). However, note that, even if GNW happens to be wrong, and the ignition event recorded in the previous experiments is not a signature of conscious access, our work still provides a mechanistic hypothesis for these large-scale cortical activity patterns (while no longer describing conscious access). It is possible to disprove our theoretical prediction by uncovering an alternative dynamic mechanism for ignition. It is also possible to disprove our mechanistic hypothesis by showing that ignition relies on a distinct neurobiological mechanism. Experimentalists can also disprove our mechanistic hypothesis by measuring NMDA fractions at inter-areal (feedforward and feedback) and local recurrent connections that are inconsistent with our prediction. Therefore, it is possible to disprove the model and to disprove GNW. However, disproving the mechanistic hypothesis of the model is not sufficient to disprove GNW.

Limitations of the study

In this study, we use a mesoscale biophysical model to investigate conscious access dynamics, adopting several structural simplifications to focus on fundamental neural processes. Notably, the model does not incorporate layer-specific cortical organization or distinctions between inhibitory cell types, both of which play distinct roles in cortical dynamics. Furthermore, neurons are represented in a simplified form, with homogeneous populations within each cortical region and without axonal delays, potentially overlooking the impact of diverse cell morphologies and conduction times on network activity. Additionally, our model uses only a subset of the macaque connectome, focusing exclusively on the cortex and omitting subcortical structures that may also contribute to conscious processing. Systematically adding these features in future versions could reveal how they interact with the core dynamics we identify here.

Conclusions

We built a connectome-based dynamic model of the primate cortex that successfully accounted for salient results on the spatio-temporal activity and behavior of primates performing tasks designed to assess conscious access. Our model predicts that feedforward excitatory connections should be dominated by AMPA receptors for rapid propagation of stimulus-related activity, while NMDA receptors in local recurrent connections and feedback projections are required for the ignition and sustained activity that accompanies conscious access. Our model reconciles seemingly contradictory anatomical and physiological data on the relative proportion of AMPA and NMDA receptors along the cortical hierarchy and takes a step toward a cross-level (bridging network, cellular, and synaptic mechanisms) theory of consciousness.

RESOURCE AVAILABILITY

Lead contact

Requests for further information and resources should be directed to and will be fulfilled by the lead contact, Xiao-Jing Wang (xjwang@nyu.edu).

Materials availability

This study did not generate new unique reagents.

Data and code availability

- The experimental data reported in this paper were published previously as part of a 2023 *Nature Neuroscience*[51] paper and are publicly available on the following platforms:
  - BALSA neuroimaging repository: P2Nql, https://balsa.wustl.edu/study/P2Nql).
  - Human Brain Project platform EBRAINS: https://doi.org/10.25493/5HK3-S8M).
- The original codes for data analyses performed in this paper are publicly available at GitHub, including method classes and Jupyter notebooks: https://github.com/ulyssek/atoum.
- Any additional information required to reanalyze the data reported in this paper is available from the lead contact upon request.

ACKNOWLEDGMENTS

This work was funded by NIH grant R01MH062349, ONR grant N00014, NSF NeuroNex grant 2015276, ONR grant N00014, James Simons Foundation grant 543057SPI, and the Swartz Foundation (to X.-J.W.); UKRI Biotechnology and Biological Sciences Research Council (BBSRC) grant BB/X013243/1 (to S.F.-W.); and NIH/NSF CRCNS grant R01MH122024 (to X.-J.W. and N.P.-G.). U.K. was supported by the European Research Council (ERC) under the European Union's Horizon 2020 Research and Innovation Program (grant agreement 866533-CORTIGRAD awarded to Daniel Margulies). S.D. was supported by Collège de France, INSERM, and CEA. N.P.-G., L.R., and M.N. were supported by the Federal Ministry of Education and Research (BMBF) under project 01GQ1902. We thank Guillermo González-Burgos for comments on an earlier draft of the manuscript. We thank Daniel Margulies for his thoughtful comments on the draft and for fostering an intellectually supportive environment during U.K.'s PhD studies. We thank the CANN lab (Bristol) and NeuroConn lab (Paris) for helpful discussions. We thank Esteban Munoz Mussat, Benoît de Courson, Julien Lie-Panis, and Aude Bernheim for the fruitful discussions and feedback that contributed to this work.

AUTHOR CONTRIBUTIONS

U.K., S.F.-W., C.S., S.D., and X.-J.W. conceived and designed the study. U.K. developed the main computational model. S.F.-W. and J.M. developed prototype models. S.F.W., J.M., D.P.B., and P.T. provided technical and theoretical guidance. M.N. and L.R. performed the experiments for the receptor density data. U.K. and S.F.-W. analyzed the computational models and experimental data. U.K. and S.F.-W. wrote and initial manuscript draft. X.-J.W., S.D., C.S., and N.P.-G. supervised the work. All authors revised and edited the manuscript.

DECLARATION OF INTERESTS

The authors declare no competing interests.

DECLARATION OF GENERATIVE AI AND AI-ASSISTED TECHNOLOGIES IN THE WRITING PROCESS

During the preparation of this work the authors used ChatGPT in order to correct typos, address grammatical mistakes, and improve readability. After using this tool/service, the authors reviewed and edited the content as needed and take full responsibility for the content of the publication.

STAR★METHODS

Detailed methods are provided in the online version of this paper and include the following:

SUPPLEMENTAL INFORMATION

Supplemental information can be found online at https://doi.org/10.1016/j.celrep.2025.115372.

Received: May 5, 2022
Revised: May 6, 2024
Accepted: February 7, 2025
Published: March 13, 2025

REFERENCES

1. James, W. (1890). Principles of Psychology. Henry Holt. https://doi.org/10.1037/10538-000.
2. Dehaene, S., Kerszberg, M., and Changeux, J.-P. (1998). A Neuronal Model of a Global Workspace in Effortful Cognitive Tasks. Proc. Natl. Acad. Sci. USA *95*, 14529. https://doi.org/10.1073/pnas.95.24.14529.
3. Lamme, V.A., and Roelfsema, P.R. (2000). The Distinct Modes of Vision Offered by Feedforward and Recurrent Processing. Trends Neurosci. *23*, 571–579. https://doi.org/10.1016/S0166-2236(00)01657-X.
4. Tononi, G. (2004). An Information Integration Theory of Consciousness. BMC. Neurosci. *5*, 42.
5. Bernard, J.B. (2005). Global Workspace Theory of Consciousness: Toward a Cognitive Neuroscience of Human Experience. Progress in brain research *150*, 45–53. https://doi.org/10.1016/S0079-6123(05)50004-9.
6. Lau, H., and Rosenthal, D. (2011). Empirical Support for Higher-Order Theories of Conscious Awareness. Trends Cogn. Sci. *15*, 365–373.
7. Aru, J., Suzuki, M., and Larkum, M.E. (2020). Cellular Mechanisms of Conscious Processing. Trends Cogn. Sci. *24*, 814–825. https://doi.org/10.1016/j.tics.2020.07.006.
8. Mashour, G.A., Roelfsema, P., Changeux, J.P., and Dehaene, S. (2020). Conscious Processing and the Global Neuronal Workspace Hypothesis. Neuron *105*, 776–798. https://doi.org/10.1016/j.neuron.2020.01.026.
9. de Lafuente, V., and Romo, R. (2005). Neuronal Correlates of Subjective Sensory Experience. Nat. Neurosci. *8*, 1698–1703. https://doi.org/10.1038/nn1587.
10. de Lafuente, V., and Romo, R. (2006). Neural Correlate of Subjective Sensory Experience Gradually Builds up across Cortical Areas. Proc. Natl. Acad. Sci. USA *103*, 14266–14271. https://doi.org/10.1073/pnas.0605826103.
11. Romo, R., and Rossi-Pool, R. (2020). Turning Touch into Perception. Neuron *105*, 16–33. https://doi.org/10.1016/j.neuron.2019.11.033.
12. Van Vugt, B., Dagnino, B., Vartak, D., Safaai, H., Panzeri, S., Dehaene, S., and Roelfsema, P.R. (2018). The Threshold for Conscious Report: Signal

Loss and Response Bias in Visual and Frontal Cortex. Science (New York, N.Y.) *360*, 537–542. https://doi.org/10.1126/science.aar7186.

13. Del Cul, A., Baillet, S., and Dehaene, S. (2007). Brain Dynamics Underlying the Nonlinear Threshold for Access to Consciousness. PLoS Biol. *5*, e260. https://doi.org/10.1371/journal.pbio.0050260.
14. Kouider, S., Stahlhut, C., Gelskov, S.V., Barbosa, L.S., Dutat, M., de Gardelle, V., Christophe, A., Dehaene, S., and Dehaene-Lambertz, G. (2013). A Neural Marker of Perceptual Consciousness in Infants. Science (New York, N.Y.) *340*, 376–380. https://doi.org/10.1126/science.1232509.
15. Dehaene, S., Naccache, L., Cohen, L., Bihan, D.L., Mangin, J.F., Poline, J.B., and Rivière, D. (2001). Cerebral Mechanisms of Word Masking and Unconscious Repetition Priming. Nat. Neurosci. *4*, 752–758. https://doi.org/10.1038/89551.
16. Sergent, C., Baillet, S., and Dehaene, S. (2005). Timing of the Brain Events Underlying Access to Consciousness during the Attentional Blink. Nat. Neurosci. *4*, 752–758. https://doi.org/10.1038/nn1549.
17. King, J.-R., and Dehaene, S. (2014). Characterizing the Dynamics of Mental Representations: The Temporal Generalization Method. Trends Cognit. Sci. *18*, 203–210. https://doi.org/10.1016/j.tics.2014.01.002.
18. Rees, G., Kreiman, G., and Koch, C. (2002). Neural Correlates of Consciousness in Humans. Nat. Rev. Neurosci. *3*, 261–270. https://doi.org/10.1038/nrn783.
19. Sadaghiani, S., Hesselmann, G., and Kleinschmidt, A. (2009). Distributed and Antagonistic Contributions of Ongoing Activity Fluctuations to Auditory Stimulus Detection. J. Neurosci. *29*, 13410–13417. https://doi.org/10.1523/JNEUROSCI.2592-09.2009.
20. Schurger, A., Sarigiannidis, I., Naccache, L., Sitt, J.D., and Dehaene, S. (2015). Cortical activity is more stable when sensory stimuli are consciously perceived. Proc. Natl. Acad. Sci. USA *112*, E2083–E2092.
21. Salti, M., Monto, S., Charles, L., King, J.R., Parkkonen, L., and Dehaene, S. (2015). Distinct cortical codes and temporal dynamics for conscious and unconscious percepts. Elife *4*, e05652.
22. Baria, A.T., Maniscalco, B., and He, B.J. (2017). Initial-State-Dependent, Robust, Transient Neural Dynamics Encode Conscious Visual Perception. PLoS Comput. Biol. *13*, e1005806. https://doi.org/10.1371/journal.pcbi.1005806.
23. Dehaene, S., Sergent, C., and Changeux, J.-P. (2003). A Neuronal Network Model Linking Subjective Reports and Objective Physiological Data during Conscious Perception. Proc. Natl. Acad. Sci. USA *100*, 8520–8525. https://doi.org/10.1073/pnas.1332574100.
24. Yang, S.-T., Wang, M., Paspalas, C.D., Crimins, J.L., Altman, M.T., Mazer, J.A., and Arnsten, A.F.T. (2018). Core Differences in Synaptic Signaling Between Primary Visual and Dorsolateral Prefrontal Cortex. Cereb. Cortex *28*, 1458–1471. https://doi.org/10.1093/cercor/bhx357.
25. Wang, X.J. (1999). Synaptic Basis of Cortical Persistent Activity: The Importance of NMDA Receptors to Working Memory. J. Neurosci. *19*, 9587–9603.
26. Wang, M., Yang, Y., Wang, C.J., Gamo, N.J., Jin, L.E., Mazer, J.A., Morrison, J.H., Wang, X.J., and Arnsten, A.F.T. (2013). NMDA Receptors Subserve Persistent Neuronal Firing during Working Memory in Dorsolateral Prefrontal Cortex. Neuron *77*, 736–749. https://doi.org/10.1016/j.neuron.2012.12.032.
27. Self, M.W., Kooijmans, R.N., Supèr, H., Lamme, V.A., and Roelfsema, P.R. (2012). Different glutamate receptors convey feedforward and recurrent processing in macaque V1. Proc. Natl. Acad. Sci. USA *109*, 11031–11036. https://doi.org/10.1073/pnas.1119527109.
28. Dehaene, S., and Changeux, J.-P. (2005). Ongoing Spontaneous Activity Controls Access to Consciousness: A Neuronal Model for Inattentional Blindness. PLoS Biol. *3*, e141–e7885. https://doi.org/10.1371/journal.pbio.0030141.
29. Joglekar, M.R., Mejias, J.F., Yang, G.R., and Wang, X.J. (2018). Inter-Areal Balanced Amplification Enhances Signal Propagation in a Large-Scale Circuit Model of the Primate Cortex. Neuron *98*, 222–234. https://doi.org/10.1016/j.neuron.2018.02.031.
30. Chaudhuri, R., Knoblauch, K., Gariel, M.A., Kennedy, H., and Wang, X.J. (2015). A Large-Scale Circuit Mechanism for Hierarchical Dynamical Processing in the Primate Cortex. Neuron *88*, 419–431. https://doi.org/10.1016/j.neuron.2015.09.008.
31. Deco, G., Kringelbach, M.L., Arnatkeviciute, A., Oldham, S., Sabaroedin, K., Rogasch, N.C., Aquino, K.M., and Fornito, A. (2021). Dynamical consequences of regional heterogeneity in the brain's transcriptional landscape. Sci. Adv. *7*, eabf4752.
32. Wong, K.-F., and Wang, X.-J. (2006). A Recurrent Network Mechanism of Time Integration in Perceptual Decisions. J. Neurosci. *26*, 1314–1328. https://doi.org/10.1523/JNEUROSCI.3733-05.2006.
33. Mejias, J.F., and Wang, X.-J. (2022). Mechanisms of Distributed Working Memory in a Large-Scale Network of Macaque Neocortex. Elife *11*, e72136. https://doi.org/10.7554/eLife.72136.
34. Elston, G.N. (2007). Specialization of the Neocortical Pyramidal Cell during Primate Evolution. In Evolution of Nervous Systems, pp. 191–242. https://doi.org/10.1016/B0-12-370878-8/00164-6.
35. Markov, N.T., Ercsey-Ravasz, M.M., Ribeiro Gomes, A.R., Lamy, C., Magrou, L., Vezoli, J., Misery, P., Falchier, A., Quilodran, R., Gariel, M.A., et al. (2014). A Weighted and Directed Interareal Connectivity Matrix for Macaque Cerebral Cortex. Cereb. Cortex *24*, 17–36. https://doi.org/10.1093/cercor/bhs270.
36. Froudist-Walsh, S., Bliss, D.P., Ding, X., Rapan, L., Niu, M., Knoblauch, K., Zilles, K., Kennedy, H., Palomero-Gallagher, N., and Wang, X.J. (2021). A Dopamine Gradient Controls Access to Distributed Working Memory in the Large-Scale Monkey Cortex. Neuron *109*, 3500–3520.e13. https://doi.org/10.1016/j.neuron.2021.08.024.
37. Sergent, C., Corazzol, M., Labouret, G., Stockart, F., Wexler, M., King, J.R., Meyniel, F., and Pressnitzer, D. (2021). Bifurcation in Brain Dynamics Reveals a Signature of Conscious Processing Independent of Report. Nat. Commun. *12*, 1149–1723. https://doi.org/10.1038/s41467-021-21393-z.
38. Dehaene, S., Changeux, J.P., Naccache, L., Sackur, J., and Sergent, C. (2006). Conscious, Preconscious, and Subliminal Processing: A Testable Taxonomy. Trends Cogn. Sci. *10*, 204–211. https://doi.org/10.1016/j.tics.2006.03.007.
39. Sergent, C., and Dehaene, S. (2003). Is Consciousness a Gradual Phenomenon? Psychol. Sci. *15*, 11–19.
40. Thorpe, S.J., and Fabre-Thorpe, M. (2001). Seeking Categories in the Brain. Science (New York, N.Y.) *291*, 260–263. https://doi.org/10.1126/science.1058249.
41. Bellet, J., Gay, M., Dwarakanath, A., Jarraya, B., van Kerkoerle, T., Dehaene, S., and Panagiotaropoulos, T.I. (2022). Decoding Rapidly Presented Visual Stimuli from Prefrontal Ensembles without Report nor Post-Perceptual Processing. Neurosci. Conscious. *2022*, niac005. https://doi.org/10.1093/nc/niac005.
42. Dehaene, S., and King, J.-R. (2016). Decoding the Dynamics of Conscious Perception: The Temporal Generalization Method. Micro-, meso-and macro-dynamics of the brain, 85–97.
43. Meyers, E.M., Freedman, D.J., Kreiman, G., Miller, E.K., and Poggio, T. (2008). Dynamic Population Coding of Category Information in Inferior Temporal and Prefrontal Cortex. J. Neurophysiol. *100*, 1407–1419. https://doi.org/10.1152/jn.90248.2008.
44. King, J.-R., Pescetelli, N., and Dehaene, S. (2016). Brain Mechanisms Underlying the Brief Maintenance of Seen and Unseen Sensory Information. Neuron *92*, 1122–1134. https://doi.org/10.1016/j.neuron.2016.10.051.
45. Steven, H.S. (2018). Nonlinear Dynamics and Chaos (CRC press).
46. Markov, N.T., Vezoli, J., Chameau, P., Falchier, A., Quilodran, R., Huissoud, C., Lamy, C., Misery, P., Giroud, P., Ullman, S., and Barone, P. (2014). Anatomy of hierarchy: feedforward and feedback pathways in

macaque visual cortex. Journal *522*, 225–259. https://doi.org/10.1002/cne.23458.

47. Impieri, D., Zilles, K., Niu, M., Rapan, L., Schubert, N., Galletti, C., and Palomero-Gallagher, N. (2019). Receptor Density Pattern Confirms and Enhances the Anatomic-Functional Features of the Macaque Superior Parietal Lobule Areas. Brain Struct. Funct. *224*, 2733–2756. https://doi.org/10.1007/s00429-019-01930-9.
48. Niu, M., Impieri, D., Rapan, L., Funck, T., Palomero-Gallagher, N., and Zilles, K. (2020). Receptor-Driven, Multimodal Mapping of Cortical Areas in the Macaque Monkey Intraparietal Sulcus. Elife *9*, e55979. https://doi.org/10.7554/eLife.55979.
49. Niu, M., Rapan, L., Funck, T., Froudist-Walsh, S., Zhao, L., Zilles, K., and Palomero-Gallagher, N. (2021). Organization of the Macaque Monkey Inferior Parietal Lobule Based on Multimodal Receptor Architectonics. Neuroimage *231*, 117843. https://doi.org/10.1016/j.neuroimage.2021.117843.
50. Rapan, L., Froudist-Walsh, S., Niu, M., Xu, T., Funck, T., Zilles, K., and Palomero-Gallagher, N. (2021). Multimodal 3D Atlas of the Macaque Monkey Motor and Premotor Cortex. Neuroimage *226*, 117574.
51. Froudist-Walsh, S., Xu, T., Niu, M., Rapan, L., Zhao, L., Margulies, D.S., Zilles, K., Wang, X.J., and Palomero-Gallagher, N. (2023). Gradients of neurotransmitter receptor expression in the macaque cortex. Nat. Neurosci. *26*, 1281–1294. https://doi.org/10.1038/s41593-023-01351-2.
52. Collins, C.E., Airey, D.C., Young, N.A., Leitch, D.B., and Kaas, J.H. (2010). Neuron densities vary across and within cortical areas in primates. Proc. Natl. Acad. Sci. USA *107*, 15927–15932.
53. Niu, M., Rapan, L., Froudist-Walsh, S., Zhao, L., Funck, T., Amunts, K., and Palomero-Gallagher, N. (2024). Multimodal mapping of macaque monkey somatosensory cortex. Prog. Neurobiol. *239*, 102633. https://doi.org/10.1016/j.pneurobio.2023.102633.
54. Markov, N.T., Ercsey-Ravasz, M., Van Essen, D.C., Knoblauch, K., Toroczkai, Z., and Kennedy, H. (2013). Cortical High-Density Counterstream Architectures. Science *342*, 1238406. https://doi.org/10.1126/science.1238406.
55. Mejias, J.F., Murray, J.D., Kennedy, H., and Wang, X.J. (2016). Feedforward and feedback frequency-dependent interactions in a large-scale laminar network of the primate cortex. Sci. Adv. *2*, e1601335.
56. Cohen, M.A., Ortego, K., Kyroudis, A., and Pitts, M. (2020). Distinguishing the Neural Correlates of Perceptual Awareness and Postperceptual Processing. J. Neurosci. *40*, 4925–4935. https://doi.org/10.1523/JNEUROSCI.0120-20.2020.
57. Dellert, T., Müller-Bardorff, M., Schlossmacher, I., Pitts, M., Hofmann, D., Bruchmann, M., and Straube, T. (2021). Dissociating the Neural Correlates of Consciousness and Task Relevance in Face Perception Using Simultaneous EEG-fMRI. J. Neurosci. *41*, 7864–7875. https://doi.org/10.1523/JNEUROSCI.2799-20.2021.
58. Pitts, M.A., Padwal, J., Fennelly, D., Martínez, A., and Hillyard, S.A. (2014). Gamma Band Activity and the P3 Reflect Post-Perceptual Processes, Not Visual Awareness. Neuroimage *101*, 337–350. https://doi.org/10.1016/j.neuroimage.2014.07.024.
59. Pitts, M.A., Lutsyshyna, L.A., and Hillyard, S.A. (2018). The Relationship between Attention and Consciousness: An Expanded Taxonomy and Implications for 'No-Report' Paradigms. Philos. Trans. R. Soc. Lond. B Biol. Sci. *373*, 20170348. https://doi.org/10.1098/rstb.2017.0348.
60. Pitts, M.A., Martínez, A., and Hillyard, S.A. (2012). Visual Processing of Contour Patterns under Conditions of Inattentional Blindness. J. Cogn. Neurosci. *24*, 287–303. https://doi.org/10.1162/jocn_a_00111.
61. Schlossmacher, I., Dellert, T., Pitts, M., Bruchmann, M., and Straube, T. (2020). Differential Effects of Awareness and Task Relevance on Early and Late ERPs in a No-Report Visual Oddball Paradigm. J. Neurosci. *40*, 2906–2913. https://doi.org/10.1523/JNEUROSCI.2077-19.2020.
62. Huang, C., Ruff, D.A., Pyle, R., Rosenbaum, R., Cohen, M.R., and Doiron, B. (2019). Circuit Models of Low-Dimensional Shared Variability in Cortical Networks. Neuron *101*, 337–348. https://doi.org/10.1016/j.neuron.2018.11.034.
63. Yoo, S.A., Martinez-Trujillo, J.C., Treue, S., Tsotsos, J.K., and Fallah, M. (2021). Feature-Based Attention Induces Surround Suppression during the Perception of Visual Motion. Preprint at bioRxiv. https://doi.org/10.1101/2021.02.17.431646.
64. Javadzadeh, M., and Hofer, S.B. (2022). Dynamic causal communication channels between neocortical areas. Neuron *110*, 2470–2483. https://doi.org/10.1016/j.neuron.2022.05.011.
65. Harrison, S.A., and Tong, F. (2009). Decoding Reveals the Contents of Visual Working Memory in Early Visual Areas. Nature *458*, 632–635. https://doi.org/10.1038/nature07832.
66. Van Kerkoerle, T., Self, M.W., and Roelfsema, P.R. (2017). Layer-specificity in the effects of attention and working memory on activity in primary visual cortex. Nat. Commun. *8*, 13804. https://doi.org/10.1038/ncomms13804.
67. Supèr, H., Spekreijse, H., and Lamme, V.A.F. (2001). A Neural Correlate of Working Memory in the Monkey Primary Visual Cortex. Science (New York, N.Y.) *293*, 120–124. https://doi.org/10.1126/science.1060496.
68. Leavitt, M.L., Mendoza-Halliday, D., and Martinez-Trujillo, J.C. (2017). Sustained Activity Encoding Working Memories: Not Fully Distributed. Trends Neurosci. *40*, 328–346. https://doi.org/10.1016/j.tins.2017.04.004.
69. Suzuki, M., and Larkum, M.E. (2020). General Anesthesia Decouples Cortical Pyramidal Neurons. Cellule *180*, 666–676.e13. https://doi.org/10.1016/j.cell.2020.01.024.
70. Takahashi, N., Ebner, C., Sigl-Glöckner, J., Moberg, S., Nierwetberg, S., and Larkum, M.E. (2020). Active Dendritic Currents Gate Descending Cortical Outputs in Perception. Nat. Neurosci. *23*, 1277–1285. https://doi.org/10.1038/s41593-020-0677-8.
71. Müller, E.J., Munn, B.R., Redinbaugh, M.J., Lizier, J., Breakspear, M., Saalmann, Y.B., and Shine, J.M. (2023). The Non-Specific Matrix Thalamus Facilitates the Cortical Information Processing Modes Relevant for Conscious Awareness. Cell Rep. *42*, 112844. https://doi.org/10.1016/j.celrep.2023.112844.
72. Whyte, C.J., Redinbaugh, M.J., Shine, J.M., and Saalmann, Y.B. (2024). Thalamic Contributions to the State and Contents of Consciousness. Neuron *112*, 1611–1625. https://doi.org/10.1016/j.neuron.2024.04.019.
73. Munn, B.R., Müller, E.J., Aru, J., Whyte, C.J., Gidon, A., Larkum, M.E., and Shine, J.M. (2023). A thalamocortical substrate for integrated information via critical synchronous bursting. Proc. Natl. Acad. Sci. USA *120*, e2308670120. https://doi.org/10.1073/pnas.2308670120.
74. Zilles, K., and Palomero-Gallagher, N. (2017). Multiple Transmitter Receptors in Regions and Layers of the Human Cerebral Cortex. Front. Neuroanat. *11*, 78. https://doi.org/10.3389/fnana.2017.00078. https://www.frontiersin.org/journals/neuroanatomy/articles/10.3389/fnana.2017.00078/full.
75. Goulas, A., Changeux, J.P., Wagstyl, K., Amunts, K., Palomero-Gallagher, N., and Hilgetag, C.C. (2021). The natural axis of transmitter receptor distribution in the human cerebral cortex. Proc. Natl. Acad. Sci. USA *118*, e2020574118. https://doi.org/10.1073/pnas.2020574118.
76. Myme, C.I.O., Sugino, K., Turrigiano, G.G., and Nelson, S.B. (2003). The NMDA-to-AMPA Ratio at Synapses Onto Layer 2/3 Pyramidal Neurons Is Conserved Across Prefrontal and Visual Cortices. J. Neurophysiol. *90*, 771–779. https://doi.org/10.1152/jn.00070.2003.
77. Feldmeyer, D., Egger, V., Lubke, J., and Sakmann, B. (1999). Reliable synaptic connections between pairs of excitatory layer 4 neurones within a single 'barrel' of developing rat somatosensory cortex. J. Physiol. *521*, 169–190. https://doi.org/10.1111/j.1469-7793.1999.00169.x.
78. Jones, K., and Baughman, R. (1988). NMDA- and non-NMDA-receptor components of excitatory synaptic potentials recorded from cells in layer V of rat visual cortex. J. Neurosci. *8*, 3522–3534. https://doi.org/10.1523/JNEUROSCI.08-09-03522.1988.

79. Kumar, S.S., and Huguenard, J.R. (2001). Properties of Excitatory Synaptic Connections Mediated by the Corpus Callosum in the Developing Rat Neocortex. J. Neurophysiol. *86*, 2973–2985. https://doi.org/10.1152/jn.2001.86.6.2973.

80. Markram, H., Lübke, J., Frotscher, M., Roth, A., and Sakmann, B. (1997). Physiology and anatomy of synaptic connections between thick tufted pyramidal neurones in the developing rat neocortex. J. Physiol. *500*, 409–440. https://doi.org/10.1113/jphysiol.1997.sp022031.

81. McBain, C., and Dingledine, R. (1992). Dual-component miniature excitatory synaptic currents in rat hippocampal CA3 pyramidal neurons. J. Neurophysiol. *68*, 16–27. https://doi.org/10.1152/jn.1992.68.1.16.

82. Umemiya, M., Senda, M., and Murphy, T.H. (1999). Behaviour of NMDA and AMPA receptor-mediated miniature EPSCs at rat cortical neuron synapses identified by calcium imaging. J. Physiol. *521*, 113–122. https://doi.org/10.1111/j.1469-7793.1999.00113.x.

83. Watt, A.J., van Rossum, M.C., MacLeod, K.M., Nelson, S.B., and Turrigiano, G.G. (2000). Activity Coregulates Quantal AMPA and NMDA Currents at Neocortical Synapses. Neuron *26*, 659–670. https://doi.org/10.1016/S0896-6273(00)81202-7.

84. Gil, Z., and Amitai, Y. (2000). Evidence for proportional synaptic scaling in neocortex of intact animals. Neuroreport *11*, 4027–4031. https://doi.org/10.1097/00001756-200012180-00025.

85. Groc, L., Gustafsson, B., and Hanse, E. (2002). Spontaneous Unitary Synaptic Activity in CA1 Pyramidal Neurons during Early Postnatal Development: Constant Contribution of AMPA and NMDA Receptors. J. Neurosci. *22*, 5552–5562. https://doi.org/10.1523/JNEUROSCI.22-13-05552.2002.

86. Seth, A. (2007). Models of Consciousness. Scholarpedia *2*, 1328–6016. https://doi.org/10.4249/scholarpedia.1328.

87. Oizumi, M., Albantakis, L., and Tononi, G. (2014). From the Phenomenology to the Mechanisms of Consciousness: Integrated Information Theory 3.0. PLoS Comput. Biol. *10*, e1003588.

88. Koch, C., Massimini, M., Boly, M., and Tononi, G. (2016). Neural Correlates of Consciousness: Progress and Problems. Nat. Rev. Neurosci. *17*, 307–321. https://doi.org/10.1038/nrn.2016.22.

89. Graziano, M.S.A., and Webb, T.W. (2015). The Attention Schema Theory: A Mechanistic Account of Subjective Awareness. Front. Psychol. *6*, 500.

90. Seth, A.K., and Hohwy, J. (2021). Predictive Processing as an Empirical Theory for Consciousness Science. Cogn. Neurosci. *12*, 89–90. https://doi.org/10.1080/17588928.2020.1838467.

91. Shea, N., and Frith, C.D. (2019). The Global Workspace Needs Metacognition. Trends Cogn. Sci. *23*, 560–571. https://doi.org/10.1016/j.tics.2019.04.007.

92. Fleming, S.M., and Lau, H.C. (2014). How to Measure Metacognition. Front. Hum. Neurosci. *8*, 443.

93. He, B.J. (2023). Towards a Pluralistic Neurobiological Understanding of Consciousness. Trends Cogn. Sci. *27*, 420–432. https://doi.org/10.1016/j.tics.2023.02.001.

94. Melloni, L., Mudrik, L., Pitts, M., and Koch, C. (2021). Making the Hard Problem of Consciousness Easier. Science (New York, N.Y.) *372*, 911–912. https://doi.org/10.1126/science.abj3259.

95. Yaron, I., Melloni, L., Pitts, M., and Mudrik, L. (2021). How Are Theories of Consciousness Empirically Tested? The Consciousness Theories Studies (ConTraSt) Database. J. Vis. *21*, 2195–7362. https://doi.org/10.1167/jov.21.9.2195.

96. Demertzi, A., Tagliazucchi, E., Dehaene, S., Deco, G., Barttfeld, P., Raimondo, F., Martial, C., Fernández-Espejo, D., Rohaut, B., Voss, H.U., et al. (2019). Human Consciousness Is Supported by Dynamic Complex Patterns of Brain Signal Coordination. Sci. Adv. *5*, eaat7603.

97. Del Cul, A., Dehaene, S., Reyes, P., Bravo, E., and Slachevsky, A. (2009). Causal Role of Prefrontal Cortex in the Threshold for Access to Consciousness. Brain *132*, 2531–2540. https://doi.org/10.1093/brain/awp111.

98. Kouider, S., and Dehaene, S. (2007). Levels of processing during non-conscious perception: a critical review of visual masking. Philos. Trans. R. Soc. Lond. B Biol. Sci. *362*, 857–875. https://doi.org/10.1098/rstb.2007.2093.

99. Kranczioch, C., Debener, S., Schwarzbach, J., Goebel, R., and Engel, A.K. (2005). Neural Correlates of Conscious Perception in the Attentional Blink. Neuroimage *24*, 704–714. https://doi.org/10.1016/j.neuroimage.2004.09.024.

100. Asplund, C.L., Fougnie, D., Zughni, S., Martin, J.W., and Marois, R. (2014). The Attentional Blink Reveals the Probabilistic Nature of Discrete Conscious Perception. Psychol. Sci. *25*, 824–831. https://doi.org/10.1177/0956797613513810.

101. Kapoor, V., Dwarakanath, A., Safavi, S., Werner, J., Besserve, M., Panagiotaropoulos, T.I., and Logothetis, N.K. (2022). Decoding internally generated transitions of conscious contents in the prefrontal cortex without subjective reports. Nat. Commun. *13*, 1535–1723. https://doi.org/10.1038/s41467-022-28897-2. https://www.nature.com/articles/s41467-022-28897-2.

102. Hesse, J.K., and Tsao, D.Y. (2020). A new no-report paradigm reveals that face cells encode both consciously perceived and suppressed stimuli. Elife *9*, e58360. https://doi.org/10.7554/eLife.58360. https://elifesciences.org/articles/58360.

103. Donahue, C.J., Sotiropoulos, S.N., Jbabdi, S., Hernandez-Fernandez, M., Behrens, T.E., Dyrby, T.B., Coalson, T., Kennedy, H., Knoblauch, K., Van Essen, D.C., and Glasser, M.F. (2016). Using Diffusion Tractography to Predict Cortical Connection Strength and Distance: A Quantitative Comparison with Tracers in the Monkey. J. Neurosci. *36*, 6758–6770.

104. Wang, X.-J. (2002). Probabilistic Decision Making by Slow Reverberation in Cortical Circuits. Neuron *36*, 955–968. https://doi.org/10.1016/S0896-6273(02)01092-9.

105. Nimchinsky, E.A., Sabatini, B.L., and Svoboda, K. (2002). Structure and Function of Dendritic Spines. Annu. Rev. Physiol. *64*, 313–353. https://doi.org/10.1146/annurev.physiol.64.081501.160008.

106. Markram, H., Lübke, J., Frotscher, M., Roth, A., and Sakmann, B. (1997). Physiology and Anatomy of Synaptic Connections between Thick Tufted Pyramidal Neurones in the Developing Rat Neocortex. J. Physiol. *500*, 409–440. https://doi.org/10.1113/jphysiol.1997.sp022031.

107. Petreanu, L., Mao, T., Sternson, S.M., and Svoboda, K. (2009). The Subcellular Organization of Neocortical Excitatory Connections. Nature *457*, 1142–1145. https://doi.org/10.1038/nature07709.

108. Nir, K., Silberberg, G., and Markram, H. (2005). The Neocortical Microcircuit as a Tabula Rasa. Proc. Natl. Acad. Sci. USA *102*, 880–885. https://doi.org/10.1073/pnas.0407088102.

109. Yuste, R., Gutnick, M.J., Saar, D., Delaney, K.R., and Tank, D.W. (1994). Ca2+ Accumulations in Dendrites of Neocortical Pyramidal Neurons: An Apical Band and Evidence for Two Functional Compartments. Neuron *13*, 23–43. https://doi.org/10.1016/0896-6273(94)90457-X.

110. Bastos, A.M., Vezoli, J., Bosman, C.A., Schoffelen, J.M., Oostenveld, R., Dowdall, J.R., De Weerd, P., Kennedy, H., and Fries, P. (2015). Visual areas exert feedforward and feedback influences through distinct frequency channels. Neuron *85*, 390–401. https://doi.org/10.1016/j.neuron.2014.12.018.

111. Song, S., Sjöström, P.J., Reigl, M., Nelson, S., and Chklovskii, D.B. (2005). Highly nonrandom features of synaptic connectivity in local cortical circuits. PLoS Biol. *3*, e68. https://doi.org/10.1371/journal.pbio.0030350.

112. Amin, Z., and Adam, K. (2015). Coordinated Neuronal Activity Enhances Corticocortical Communication. Neuron *87*, 827–839. https://doi.org/10.1016/j.neuron.2015.07.026. https://www.cell.com/neuron/fulltext/S0896-6273(15)00648-0.

113. Yang, G.R., Murray, J.D., and Wang, X.-J. (2016). A Dendritic Disinhibitory Circuit Mechanism for Pathway-Specific Gating. Nat. Commun. *7*, 12815. https://doi.org/10.1038/ncomms12815.

114. Abbott, L.F., and Chance, F.S. (2005). Drivers and Modulators from Push-Pull and Balanced Synaptic Input. Prog. Brain. Res. *149*, 147–155. https://doi.org/10.1016/S0079-6123(05)49011-1.

115. Rapan, L., Froudist-Walsh, S., Niu, M., Xu, T., Zhao, L., Funck, T., Wang, X.J., Amunts, K., and Palomero-Gallagher, N. (2023). Cytoarchitectonic, receptor distribution and functional connectivity analyses of the macaque frontal lobe. Elife *12*, e82850.

116. Rapan, L., Niu, M., Zhao, L., Funck, T., Amunts, K., Zilles, K., and Palomero-Gallagher, N. (2022). Receptor Architecture of Macaque and Human Early Visual Areas: Not Equal, but Comparable. Brain Struct. Funct. *227*, 1247–1263. https://doi.org/10.1007/s00429-021-02437-y.

117. Björn, M. (1983). Silver Staining of Cell Bodies by Means of Physical Development. J. Neurosci. Methods *9*, 235–241. https://doi.org/10.1016/0165-0270(83)90086-9.

118. Palomero-Gallagher, N., and Zilles, K. (2018). Chapter 24 - Cyto- and Receptor Architectonic Mapping of the Human Brain. Handb. Clin. Neurol. *150*, 355–387. https://doi.org/10.1016/B978-0-444-63639-3.00024-4.

119. Lebarbier, E., and Mary-Huard, T. (2004). Le Critère BIC: Fondements Théoriques et Interprétation (INRIA). PhD thesis.

120. Pedregosa, F., Varoquaux, G., Gramfort, A., Michel, V., and Thirion, B. (2011). Scikit-Learn: Machine Learning in Python. the Journal of machine Learning research *12*, 2825–2830.

STAR★METHODS

KEY RESOURCES TABLE

REAGENT or RESOURCE	SOURCE	IDENTIFIER
Deposited data		
in vivo autoradiography data	BALSA	https://balsa.wustl.edu/study/P2Nql
in vivo autoradiography data	EBRAINS	https://doi.org/10.25493/5HK3-S8M
Software and algorithms		
Brian2	Brian2 Project Team	https://brian2.readthedocs.io/en/stable/
Connectome-Based Model	Github	https://github.com/ulyssek/atoum

METHOD DETAILS

Model overview

We developed a connectome-based dynamical model of the macaque cortex to investigate the synaptic and network mechanisms underlying the ignition of distributed neural activity that accompanies conscious perception. We simulated local cortical circuits at each of 40 cortical areas and set the existence and strength of directed connections between areas using retrograde tract-tracing data. Cortical areas differed based on their inter-areal connectivity and dendritic spine count on pyramidal cells. As a starting point, we adapted a recently developed model of distributed working memory in 30 cortical areas.[33]

Retrograde tract-tracing data

The inter-areal connectivity data in this paper was acquired by Henry Kennedy and colleagues as part of an ongoing effort to map the cortical mesoscopic connectome of the macaque using retrograde tract-tracing.[35,46,54,55] Here we use the directed, weighted connectivity data between 40 cortical areas, which is the most recent release.[36]

A few details of how the connectivity data was collected and processed will help the reader understand the connectome-based dynamical model. For each target area, a retrograde tracer was injected into the cortex. The tracer was taken up in the axon terminals in this area, and retrogradely transported to the cell bodies of neurons that projected to the target. The cortical areas (l) that send axons to the target area (k) are called source areas. For a given injection, all marked cell bodies in the cortex outside of the injected (target) area was counted as labeled neurons. The number of labeled neurons (LN) within a source cortical area was then divided by the number of labeled neurons in the whole cortex (excluding the target area), to give a fraction of labeled neurons (FLN). The FLN was averaged across all injections in a given target area. For this calculation, we include all cortical areas ($n^{areas} = 91$) defined in the Lyon atlas.[35]

$$FLN_{[k,l]} = \frac{LN_{[k,l]}}{\sum_{l=1}^{n^{areas}} LN_{[k,l]}} \quad \text{(Equation 1)}$$

Note that there are 91 cortical areas in the Lyon atlas, and currently 40 areas have been injected with retrograde tracers. This gives the connection strength from all 91 areas to the 40 injected areas, and the full bidirectional connectivity of a subgraph of 40 areas. We use this 40-area subgraph as an anatomical basis for the dynamical model.

In addition, for each inter-areal connection we defined the supragranular labeled neurons (SLN) as the fraction of neurons in the source area whose cell bodies were in the superficial (aka supragranular) layers.

$$SLN_{[k,l]} = \frac{LN^{supra}_{[k,l]}}{LN^{supra}_{[k,l]} + LN^{infra}_{[k,l]}} \quad \text{(Equation 2)}$$

The subiculum (SUB) and piriform cortex (PIR) have a qualitatively different laminar structure to the neocortical areas, and therefore supra- and infra-laminar connections (and thus the SLN) from these areas are undefined. We removed all connections from these areas from the following calculations ($n^{areas,SLN} = 89$). These connectivity data are available on the core-nets website (register, click the "Download" button, and select the data associated with[36]).

Dendritic spine data

The spine count data were taken from a series of studies by Elston and colleagues[34] and mapped onto the Yerkes19 cortical surface,[103] as described in.[36,51] Locations on the Yerkes19 cortical surface are represented by 32,492 vertices. The spine count data was obtained by Elston and colleagues from 27 injection sites across the cortex. For each injection site we estimated the number of vertices overlapping with each area in the Lyon atlas. If a cortical area contained only one injection site, the mean spine count

from pyramidal cells in that site was taken as the spine count for the area. If a cortical area contained multiple injection sites, we performed a weighted average of the spine counts, according to the number of vertices of overlap. In this way we estimated the spine counts on pyramidal cells in 24 of the 40 injected regions in the Lyon atlas. Based on the strong positive correlation between spine count and cortical hierarchy (r = 0.61, p = 0.001), and following previous work,[30,33,36] we inferred the spine count for the remaining regions based on the hierarchy using linear regression.

Local cortical circuit architecture

In each cortical area we simulated a local circuit, with two interacting excitatory populations (E_1 and E_2), and one population of inhibitory (I) neurons. This is based on a mean-field reduction of a spiking neural network model of cortex.[32,104]

Description of dynamical variables

The neural populations interact via synapses that contain NMDA, AMPA and GABA receptors. Each receptor has its own dynamics, governed by the following equations.

The synaptic variables are updated as follows[25,32]

$$\frac{ds^{NMDA}}{dt} = -\frac{s^{NMDA}}{\tau^{NMDA}} + \left(1 - s^{NMDA}\right)\gamma_{NMDA} r_E \quad \text{(Equation 3)}$$

$$\frac{ds^{AMPA}}{dt} = -\frac{s^{AMPA}}{\tau^{AMPA}} + \left(1 - s^{AMPA}\right)\gamma_{AMPA} r_E \quad \text{(Equation 4)}$$

$$\frac{ds^{GABA}}{dt} = -\frac{s^{GABA}}{\tau^{GABA}} + \gamma_{GABA} r_I \quad \text{(Equation 5)}$$

where s is the fraction of open synaptic ion channels due to bound receptors, τ is the time constant of decay of that receptor and γ_{NMDA}, γ_{AMPA} and γ_{GABA} are constants. r_E and r_I are the firing rates of the presynaptic excitatory and inhibitory cells that stimulate the NMDA, AMPA and GABA receptors, calculated below.

NMDA/AMPA ratio

We explored the effects of different NMDA/(NMDA+AMPA) fractions, κ, at local and long-range feedforward and feedback connections. The values used for the main simulations, unless otherwise stated, are in Table S1.

Modulation of excitatory connections by dendritic spines

Approximately 90% of excitatory synapses on neocortical pyramidal cells are on dendritic spines.[105] On this basis, we modulate the strength of excitatory connections according to the dendritic spine count.

$$\chi_{[k]} = \frac{\chi^{raw}_{[k]} - \chi^{raw}_{\min}}{\chi^{raw}_{\max} - \chi^{raw}_{\min}}$$

for all cortical areas $[k]$. $\chi^{raw}_{[k]}$ is the spine count for area $\chi^{raw}_{[k]}$, and $\chi^{raw}_{\min}$ and $\chi^{raw}_{\max}$ are the minimum and maximum spine counts observed in the data. $\chi_{[k]}$ is therefore the spine count of area k rescaled to lie in the [0,1] range.

We then apply the gradient of excitation as follows.

$$z_{E,[k]} = z^{\min} + \chi_{[k]}\left(1 - z^{\min}\right) \quad \text{(Equation 6)}$$

where $z^{\min}$ sets the lower bound for the modulation of excitatory connections by the spine count, χ. $z_{E,[k]}$ therefore defines how spine count modulates excitatory connections in area k.

Description of local currents

The local NMDA current onto each population $Ei \in \{E_1, E_2\}$ in area $[k]$ is calculated as follows

$$I^{NMDA,local}_{Ei,[k]} = z_{E,[k]}\kappa^{local} G^{NMDA,loc}_{E,E} s^{NMDA}_{Ei,[k]} \quad \text{(Equation 7)}$$

Where $z_{E,[k]}$ is the dendritic spine count gradient, κ^{local} the NMDA receptor fraction of the postsynaptic population, $G^{NMDA,loc}_{E,E}$ the local NMDA coupling from the population to itself.

Local connections tend to target the perisomatic area (soma and proximal dendrites) of pyramidal cells.[106–108] The soma and proximal dendrites act as a single functional compartment that is separate from a distal dendritic compartment.[109] As our dendritic function F (described below) models this distal dendritic compartment, we do not pass local excitatory connections through F.

Similarly local excitatory connections via the AMPA receptors are scaled by the AMPA receptor fraction $1 - \kappa^{local}$, the dendritic spine count gradient $z_{E,[k]}$, and $G_{E,E}^{AMPA,loc}$ the local AMPA coupling from the population to itself.

$$I_{Ei,[k]}^{AMPA,local} = z_{E,[k]}\left(1 - \kappa^{local}\right)G_{E,E}^{AMPA,loc}s_{Ei,[k]}^{AMPA} \quad \text{(Equation 8)}$$

Local inhibitory connections are not directly modulated by the dendritic spine count (as spines indicate excitatory synapses on pyramidal cells,[105]).

$$I_{Ei,[k]}^{GABA} = G_{E,I}^{GABA}s_{[k]}^{GABA} \quad \text{(Equation 9)}$$

Where $G_{E,I}^{GABA}$ is the connection strength from the inhibitory pool to the excitatory pools.

In order to keep the spontaneous activity level similar across brain areas, the local NMDA input to the I population increases with the spine count, and is defined as follows[33]

$$I_{I,[k]}^{NMDA,local} = z_{I,[k]}G_{I,E}^{NMDA,loc}\sum_{Ei\epsilon\{E_1,E_2\}}s_{Ei,[k]}^{NMDA} \quad \text{(Equation 10)}$$

with

$$z_{I,[k]} = z_I^{\min} + \chi_{[k]}\left(1 - z_I^{\min}\right) \quad \text{(Equation 11)}$$

For the Main Figures in the manuscript, there is no local AMPA current targeting the inhibitory population. However, including AMPA input to inhibitory cells does not significantly change the results.

Description of noise, background and vigilance currents

Noise is modeled as an Ornstein-Uhlenbeck process, separately for each population i in E1,E2,I.

$$dI_i^{noise}(t) = -\frac{1}{\tau^{AMPA}}I_i^{noise}(t)dt + \eta(t)\sigma_{i,noise} \quad \text{(Equation 12)}$$

where $\sigma_{i,noise}$ is the standard deviation of the noise and η is Gaussian white noise with zero mean and unit variance.

A constant background current I_i^{bg} was also added to each population (Table S1). This represents input from brain areas that are not explicitly modeled.

In addition, we examined the effect of an extra, weak excitatory current, I^{vig}, to each unit in associative areas (top 75% of areas ranked according to the hierarchy), which simulated the effect of vigilance on the model.[23,28,71–73]

As a simplification, each of these currents targets the perisomatic compartment (i.e., it is not passed through the distal dendritic function F).

Large-scale connectivity structure

In the model, cortical areas are connected using connectivity strengths derived from the retrograde tract-tracing data. The long-range connectivity matrices are built from the FLN matrix. However, as noted in,[35,46,55] the FLN matrix spans 5 orders of magnitude. The relationship between anatomical and physiological connectivity strengths is not clear, but if we were to use the raw FLN values in the large-scale model, many of the weaker connections would become irrelevant. To deal with this, we follow[55,33] and rescale the FLN matrix in order to increase the influence of smaller connections while maintaining the topological structure.[55] found this rescaling was necessary to reproduce the significant inter-areal interactions found in,[110] and give a range of effective connectivity values similar to previous estimates.[111]

$$w_{[k,l]} = \frac{FLN_{[k,l]}^{b_1}}{\sum_{l=1}^{n^{sub}}FLN_{[k,l]}^{b_1}} \quad \text{(Equation 13)}$$

Here we restrict calculations to the injected cortical areas i, j, which allows us to simulate the complete bidirectional connectivity structure within the subgraph ($n^{sub} = 40$). Note that intra-areal connections are not quantified in the dataset. We use the same parameter value $b1$ as in[55,33] (Table S1) to construct our inter-areal connectivity matrix.

Calculation of long-range currents

Excitatory cells in different cortical areas with the same receptive fields are more likely to be functionally connected.[112] This is reflected in our model as follows. In the source area, there are two excitatory populations, 1 and 2, each sensitive to a particular feature of a visual stimulus (such as a location in the visual field). Likewise in the target area, there are two populations 1 and 2, sensitive to the same visual features. We assume that the output of population 1 in the source area goes to population 1 in the target area, and the output of population 2 in the source area goes to population 2 in the target area.

The total long-range connections mediated by the NMDA receptors on the excitatory population E_i in area $[k]$ is calculated as follows:

$$I_{E_i[k]}^{NMDA,LR} = G_E^{NMDA} z_{E,[k]} \left(\sum_{l=1}^{n^{sub}} w_{[k,l]} \left(SLN_{[k,l]} \kappa_N^{sup} \rho_E^{sup} + (1 - SLN_{[k,l]}) \kappa_N^{dp} \rho_E^{dp} \right) s_{Ei[l]}^{NMDA} \right) \quad \text{(Equation 14)}$$

See below for further details:

$$I_{E_i[k]}^{NMDA,LR} = G_E^{NMDA} z_{E,[k]} \left(\sum_{l=1}^{n^{sub}} w_{[k,l]} \left(SLN_{[k,l]} \kappa_N^{sup} \rho_E^{sup} + (1 - SLN_{[k,l]}) \kappa_N^{dp} \rho_E^{dp} \right) s_{Ei[l]}^{NMDA} \right)$$

The amount of long-range current onto the excitatory population E_i in area k that comes via NMDA receptors depends on the fraction of open synaptic ion channels due to occupied NMDA receptors and the anatomical strength of inter-areal connections from all source areas l that target area k. This is scaled by the global excitatory NMDA coupling strength and the amount of dendritic spines per pyramidal cell (i.e. excitatory synapses) in area k. We separate the superficial layer from the deep layer projections as they may be mediated by different receptor types and target different cell types.

Equations 16, 17, 18, and 19 can be understood similarly. Note that distinct layers were not explicitly simulated in the model. However, in the real brain, connections from superficial and deep layers may have different impacts on brain dynamics. Therefore, we allowed the cell-type targets and receptors mediating interareal connections from superficial and deep layers to be variables. We investigate the impact of modifying these variables in Figure 2.

To be precise, G_E^{NMDA} is the global coupling for NMDA-mediated inter-areal connections, $z_{E,[k]}$ is the dendritic spine count value for area k (as defined above), $w_{[k,l]}$ is the anatomical connection strength from area l to area k, $SLN_{[k,l]}$ is the fraction of neurons projecting from area l to area k that have their cell bodies in the superficial layers (as above), κ_N^{sup} is the fraction of excitation that is mediated by NMDA receptors for connections from superficial layers, ρ_E^{sup} is the fraction of superficial layer projections targeting excitatory cells and $s_{[l]}^{NMDA}$ is the NMDA synaptic gating variable from the corresponding excitatory population in source area l. Similarly, κ_N^{dp} is the fraction of excitation from deep layer projections mediated by NMDA receptors, and ρ_E^{dp} is the fraction of deep layer projections targeting excitatory cells. $i = 1, 2$ denotes the excitatory population.

Long-distance connections tend to target more distal parts of the dendrites,[107] which act as a functionally separate compartment from the perisomatic area.[109] For this reason, we pass the long-distance connections through the dendritic function F before they reach the soma.

Similarly, the total long-range connections of the excitatory population in area $[k]$ mediated by AMPA receptors is calculated as follows:

$$I_{Ei[k]}^{AMPA,LR} = G_E^{AMPA} z_{E,[k]} \left(\sum_{l=1}^{n^{sub}} w_{[k,l]} \left(SLN_{[k,l]} (1 - \kappa_N^{\text{sup}}) \rho_E^{\text{sup}} + (1 - SLN_{[k,l]}) (1 - \kappa_N^{dp}) \rho_E^{dp} \right) s_{Ei[l]}^{AMPA} \right) \quad \text{(Equation 15)}$$

where $(1 - \kappa_N^{\text{sup}})$ and $(1 - \kappa_N^{dp})$ are the fraction of inter-areal connections from superficial and deep layers mediated by *AMPA* receptors. This is scaled by the global excitatory AMPA coupling strength (G_E^{AMPA}).

The total excitatory long-range current in then computed as follow:

$$I_{Ei[k]}^{LR} = F\left(I_{Ei[k]}^{NMDA,LR} + I_{Ei[k]}^{AMPA,LR} \right) \quad \text{(Equation 16)}$$

The function F is a simplification of a dendritic function used in previous local and large-scale models.[36,113] It helps the network stabilize, and avoid epileptic behaviors.

$$F(X) = \left\{ \begin{array}{cc} 0pA & \text{for } X \leq 0pA \\ 300pA, & \text{for } X \geq 300pA \\ X, & \text{otherwise} \end{array} \right\} \quad \text{(Equation 17)}$$

The total long-range connections targeting inhibitory population in area $[k]$ that are mediated by NMDA receptors is calculated as follows:

$$I_{I[k]}^{NMDA,LR} = G_I^{NMDA} z_{I,[k]} \left(\sum_{l=1}^{n^{sub}} w_{[k,l]} \left(SLN_{[k,l]} \kappa_N^{\text{sup}} (1 - \rho_E^{\text{sup}}) + (1 - SLN_{[k,l]}) \kappa_N^{dp} (1 - \rho_E^{dp}) \right) s_{[l]}^{NMDA} \right) \quad \text{(Equation 18)}$$

where $(1 - \rho_E^{\text{sup}})$ and $(1 - \rho_E^{dp})$ are the fraction of feedforward and feedback inter-areal connections targeting inhibitory cell populations. We assume different effective strengths for long-range connections targeting excitatory and inhibitory pools, captured by G_I^{NMDA} and G_I^{AMPA}. Although cortical inhibitory interneurons do not contain dendritic spines, we assume that the level of excitation onto inhibitory scales similarly with the spine count. This has been shown to be an effective way of maintaining spontaneous activity levels across areas.[33]

The total long-range connections targeting the inhibitory population in area $[k]$ that are mediated by AMPA receptors is calculated as:

$$I_{I[k]}^{AMPA,LR} = G_I^{AMPA} z_{I,[k]} \left(\sum_{I=1}^{n^{sub}} w_{[k,J]} \left(SLN_{[k,J]} (1 - \kappa_N^{sup})(1 - \rho_E^{sup}) + (1 - SLN_{[k,J]})(1 - \kappa_N^{dp})(1 - \rho_E^{dp}) \right) s_{[J]}^{AMPA} \right) \quad \text{(Equation 19)}$$

with all variables as described above.

Application of external stimuli for tasks

In all simulations, the stimulus is applied for 50ms to excitatory population 1 in area V1. In the brain, visual input from LGN to V1 targets layer IV local excitatory neurons, which then excite the perisomatic areas of layer III pyramidal cells. For this reason we model external input to the perisomatic compartment of excitatory neurons in V1 (i.e., it is not passed through the dendritic function F). In all equations, the stimulus is designated by the term I^{stim}.

Total current in large-scale model

The total current for each neural population E_i in each area k equals the sum of all long-range, local and external inputs, and intrinsic currents,

$$I_{E_i[k]}^{total} = F\left(I_{E_i[k]}^{NMDA,LR}\right) + F\left(I_{E_i[k]}^{AMPA,LR}\right) + I_{E_i[k]}^{NMDA,local} + I_{E_i[k]}^{AMPA,local} + I_{E_i[k]}^{GABA,local} + I_{E_i[k]}^{noise} + I_{E_i}^{bg} + I_{E_i[k]}^{stim} + I_{E_i[k]}^{vig} \quad \text{(Equation 20)}$$

$$I_{I[k]}^{total} = I_{I[k]}^{NMDA,LR} + I_{I[k]}^{AMPA,LR} + I_{I[k]}^{NMDA,local} + I_{I[k]}^{AMPA,local} + I_{I[k]}^{GABA,local} + I_{I[k]}^{noise} + I_I^{bg} \quad \text{(Equation 21)}$$

where $i \epsilon \{1, 2\}$, (E1: excitatory population 1; E2: excitatory population 2; I: inhibitory population).

Description of f-I curves

The f-I (current to frequency) curve of the excitatory population is

$$f\left(I_E^{total}\right) = \frac{a I_E^{total} - b}{1 - e^{-d\left(a I_E^{total} - b\right)}} \quad \text{(Equation 22)}$$

where I_E^{total} is the total input to the population, a is a gain factor, d determines the curvature of $f(I_E^{total})$, such that if d is large, $f(I_E^{total})$ acts like a threshold-linear function, with threshold b.[114]

The f-I curves for the inhibitory neuron populations are modeled using a threshold-linear function

$$f\left(I_I^{total}\right) = \begin{cases} \beta_i \left(I_I^{total} - I_{th}\right) & \text{for } I_I^{total} \geq I_{th} \\ 0, & \text{otherwise} \end{cases} \quad \text{(Equation 23)}$$

where I_I^{total} is the total input to the population, β_i is the gain and I_{th} is the threshold.

See Table S1 for parameter values.

The firing rates are updated as follows

$$\tau^r \frac{dr}{dt} = -r + f\left(I^{total}\right) \quad \text{(Equation 24)}$$

for all cell types.

In-vitro receptor autoradiography

Quantitative *in-vitro* receptor autoradiography was applied to determine the densities of NMDA and receptors in cytoarchitectonically identified cortical areas of the macaque monkey brain.[47–50,115,116]

Brain tissue was shock frozen at −40°C in isopentane, hemispheres serially sectioned in the coronal plane at 20μm by means of a cryomicrotome, and sections thaw mounted onto glass slides. Alternating sections were processed for the visualization of cell bodies[117] or of receptor densities according to previously published established protocols ([118]; Table S2). In short, receptor incubation protocols consisted of a preincubation to rehydrate sections and remove endogenous ligands, a main incubation, and a washing step to stop the binding process and remove surplus ligand and buffer salts. The main incubation encompassed parallel experiments to identify the total and non-specific binding of each ligand, whereby sections were incubated with the radiolabeled ligand alone or with the radiolabeled ligand in conjunction with a non-labelled displacer, respectively.

Radiolabeled sections were co-exposed with plastic standards calibrated to account for total brain protein content and with known concentrations of radioactivity against tritium (3H) sensitive films. The ensuing autoradiographs were digitized with an 8-bit gray value resolution for densitometric analysis (Palomero-Gallagher and Zilles, 2018). Hereby, calibration curves computed by non-linear, least-squares fitting were used to define the relationship between gray values and concentrations of radioactivity derived from

the plastic standards. Radioactivity concentrations (*R*; in counts per minute, cpm) were converted to binding site concentrations (*Cb*; in fmol/mg protein) using the following equation:

$$C_b = \frac{R}{E \cdot B \cdot W_b \cdot S_a} \cdot \frac{K_D + L}{L} \quad \text{(Equation 25)}$$

Where *E* is the efficiency of the scintillation counter, *B* is a constant representing the number of decays per unit of time and radioactivity (Ci/min), *Wb* the protein weight of a standard (mg), *Sa* the specific activity of the ligand used to label the target receptor (Ci/mmol), K_D the dissociation constant of the ligand (nM), and *L* the concentration of the ligand in the main incubation buffer (nM; determined by scintillation). Thus, the gray value of each pixel in a receptor autoradiograph could be transformed into a receptor density in fmol/mg protein. The location and extent of each cytoarchitectonically identified area was transferred to the neighboring autoradiographs and, for each receptor type separately, the mean (averaged over all cortical layers) of the gray values contained in 3-5 sections of the area in question was transformed into a receptor concentration per unit protein (fmol/mg protein).

Receptor data-based model

For the receptor data-based model, we matched the total NMDA fraction to that seen in the data, adjusting for a constant mean shift between the model and receptor data, which we assume to be due to unmodelled connections (e.g., background inputs).

We calculate the overall NMDA fraction $X_{[k],model}$ (fraction of NMDA receptors over total number of excitatory receptors) in each area of the model.

$$X_{[k],model} = NMDA_{[k]} \,/\, \left(NMDA_{[k]} + AMPA_{[k]}\right) \quad \text{(Equation 26)}$$

where $NMDA_k$ and $AMPA_k$ are the total local and inter-areal connections mediated by each receptor type.

Here

$$NMDA_k = N^{loc}_{[k]} + N^{lr}_{[k]} \quad \text{(Equation 27)}$$

$$NMDA_k = N^{loc}_{[k]E,E} + N^{loc}_{[k]I,E} + N^{lr}_{[k]E,E} + N^{lr}_{[k]I,E} \quad \text{(Equation 28)}$$

With.

$N^{loc}_{[k]E,E}$ the number of NMDA receptors on the excitatory neurons coming from local connections.

$N^{loc}_{[k]I,E}$ the number of NMDA receptors on the inhibitory neurons coming from local connections.

$N^{lr}_{[k]}$ the total number of NMDA receptors coming from long-range connections.

$N^{lr}_{[k]E,E}$ the number of NMDA receptors on the excitatory neurons coming from long-range connections.

$N^{lr}_{[k]I,E}$ the number of NMDA receptors on the inhibitory neurons coming from long-range connections.

In the model, $G^{NMDA,loc}_{E,E}$ and $G^{AMPA,loc}_{E,E}$ are set as follow:

$$\frac{G^{NMDA,loc}_{E,E}}{g^{NMDA}} = \frac{G^{AMPA,loc}_{E,E}}{g^{AMPA}} = G^{loc}_{E,E} \quad \text{(Equation 29)}$$

With g^{NMDA} the conductance due to one bound NMDA receptor and g^{AMPA} the conductance due to one bound AMPA receptor. We also define:

$$\frac{G^{NMDA,loc}_{I,E}}{g^{NMDA}} = G^{loc}_{I,E} \quad \text{(Equation 30)}$$

This equations can be expanded based on Equations 7, 10, 14, and 17

$$\begin{aligned} NMDA_k = {} & z_{E,[k]} \kappa^{loc} G^{loc}_{E,E} \\ & + z_{I[k]} G^{loc}_{I,E} \\ & + z_{E,[k]} G^{lr}_{E,E} \sum_{l=1}^{n^{sub}} w_{[k,l]} \left(SLN_{[k,l]} \kappa^{\sup} \rho^{\sup} + \left(1 - SLN_{[k,l]}\right) \kappa^{dp} \rho^{dp}\right) \\ & + z_{I[k]} G^{lr}_{I,E} \sum_{l=1}^{n^{sub}} w_{[k,l]} \left(SLN_{[k,l]} \kappa^{\sup} \left(1 - \rho^{\sup}\right) + \left(1 - SLN_{[k,l]}\right) \kappa^{dp} \left(1 - \rho^{dp}\right)\right) \end{aligned} \quad \text{(Equation 31)}$$

In the reference model, used throughout Figures 1, 2, 3, 4, 5 and 6 κ^{loc} is the same across all cortical areas.

Similarly:

$$AMPA_k = A^{loc}_{[k]E,E} + A^{lr}_{[k]} \quad \text{(Equation 32)}$$

$$AMPA_k = A^{loc}_{[k]E,E} + A^{lr}_{[k]E,E} + A^{lr}_{[k]I,E} \quad \text{(Equation 33)}$$

It is worth noting that their are no local AMPA connections targeting the inhibitory pool.

$$\begin{aligned} AMPA_k = {} & z_{E,[k]}\left(1-\kappa^{loc}\right)G^{loc}_{E,E} \\ & + z_{E,[k]}G^{lr}_{E,E}\sum_{I=1}^{n^{sub}} w_{[k,I]}\left(SLN_{[k,I]}(1-\kappa^{\text{sup}})\rho^{\text{sup}} + \left(1-SLN_{[k,I]}\right)\left(1-\kappa^{dp}\right)\rho^{dp}\right) \\ & + z_{I[k]}G^{lr}_{I,E}\sum_{I=1}^{n^{sub}} w_{[k,I]}\left(SLN_{[k,I]}(1-\kappa^{\text{sup}})(1-\rho^{\text{sup}}) + \left(1-SLN_{[k,I]}\right)\left(1-\kappa^{dp}\right)\left(1-\rho^{dp}\right)\right) \end{aligned} \quad \text{(Equation 34)}$$

In practice, both $NMDA_k$ and $AMPA_k$ should be doubled (to represent the two excitatory populations), but as this affects all terms in the numerator and denominator, it will not affect the fraction $X_{[k]}$.

We show in Figure 2 how the proportion of superficial and deep layer projections mediated by AMPA and NMDA receptors should lie in a particular range in order to enable rapid 'ignition' of cortical activity. Therefore, for the receptor data-based model, we treat these long-range feedforward and feedback NMDA and AMPA fractions as fixed. We then set the overall NMDA fraction in each area to match the experimentally-measured value $X_{[k],data}$, shifted by a constant term c to account for the a mean shift between the raw receptor data and the reference model used in the rest of the paper. We can then calculate the local NMDA fraction $\kappa^{local}_{[k]}$ in each area required to match the observed NMDA fraction distribution across the cortex.

By reorganising Equations 26, 27, 28, 29, 30, 31, 32, 33, and 34, we can compute the local fraction $\kappa^{local}_{[k]}$ as a function of network parameters and real receptor data $X_{[k],data}$. We forced $\kappa^{local}_{[k]}$ to lie between 0 and 1 using a clip function.

QUANTIFICATION AND STATISTICAL ANALYSIS

Classification of model dynamics

This section corresponds to the analysis in Figure 3A.

Model 0: Null model

In this model, the external input has no effect on the activity. Irrespective of whether a stimulus was presented or not, and irrespective of its strength, activity follows a Gaussian distribution centered on μ with a standard deviation of σ.

$$p_0(activity = x|I_{stim} = I) = \frac{1}{\sigma\sqrt{2\pi}}\, e^{-\frac{(x-\mu)^2}{2\sigma^2}} \quad \text{(Equation 35)}$$

There are two free parameters: μ and σ

Model 1: Unimodal non-linear

In this model, the activity evoked for each stimulus strength I follows a Gaussian distribution centered on a mean μ - following a sigmoid function of I - and a standard deviation σ, following a linear function of the mean μ. For this model, the probability to reach activity level x for an input I is given by:

$$p_1(activity = x|I_{stim} = I) = \frac{1}{\sigma(I)\sqrt{2\pi}}\, e^{-\frac{(x-\mu(I))^2}{2\sigma(I)^2}} \quad \text{(Equation 36)}$$

with

$$\mu(I) = \frac{\mu_{\max} - \mu_{\min}}{1+e^{-k(I-I_0)}} + \mu_{\min} \quad \text{(Equation 37)}$$

and

$$\sigma(I) = \sigma_{slope}\mu(I) + \sigma_{intercept} \quad \text{(Equation 38)}$$

There are six free parameters: $\mu_{\max}$, $\mu_{\min}$, k, I_0, σ_{slope} and $\sigma_{intercept}$

Model 2: Bifurcation

In this model, the activity evoked for each stimulus strength I has a probability $\beta(I)$ to belong to a high state (Gaussian distribution centered on μ_{high} of variance σ_{high}), and a probability $(1-\beta(I))$ to belong to a low state (Gaussian distribution centered

on μ_{low} of variance σ_{low}, the baseline activity observed in the absence of stimulation). For this model, the probability to reach activity level x for an input I is given by:

$$p_2(activity = x|I_{stim} = I) = \beta(I)\left(\frac{1}{\sigma_{high}\sqrt{2\pi}}\ e^{-\frac{\left(x-\mu_{high}\right)^2}{2\sigma_{high}^2}}\right)$$

$$+(1-\beta(I))\left(\frac{1}{\sigma_{low}\sqrt{2\pi}}\ e^{-\frac{(x-\mu_{low})^2}{2\sigma_{low}^2}}\right) \quad \text{(Equation 39)}$$

with

$$\beta(I) = \frac{1}{1+e^{-k(I-I_0)}} \quad \text{(Equation 40)}$$

There are six free parameters: μ_{high}, μ_{low}, σ_{high}, σ_{low}, k and I_0

Bayesian model comparison

We compared the performance of the different models simulating 100 simulations for four different input current values (400 trials in total). The activity was sampled every 40ms and the activity was averaged over all 40 areas. The best parameters for each model were estimated by maximum likelihood, i.e., by finding the parameters maximizing the product of the likelihoods across the different trials (or, equivalently, maximizing the sum of the log likelihoods). The parameter search was achieved using the scipy.optimize function. In order to compare our different models, we used the following formula, where $P(M_i|x(t))$ is the posterior probability of the model $i \in \{0,1,2\}$ at the time step t.[119]

$$P(M_i|x(t)) = \frac{e^{\frac{BIC_i(t) - MIN_{i\in\{0,1,2\}}(BIC_i(t))}{2}}}{\sum_{i\in\{0,1,2\}} e^{\frac{BIC_i(t) - MIN_{i\in\{0,1,2\}}(BIC_i(t))}{2}}} \quad \text{(Equation 41)}$$

where $BIC_i(t)$ correspond to the Bayesian Information Criterion of model i at time step t for the best parameter set of this model.

Temporal generalization of stimulus detection decoders

This section corresponds to the analysis in Figures 3B–3E.

To decode the trial outcome from instantaneous trial activity patterns, we first separated the data from 400 trials into a training set (300 trials) and a test set (100 trials). All trials received a near-threshold (50% detection rate) stimulus input to population E1 of area V1. The combined training and test set contained 200 hit and 200 miss trials, and these were randomly shuffled and allocated to the training and test sets.

As activity in region 9/46d was used to readout the trial outcome, we trained the classifier on activity in all other areas. Trials were considered a 'Hit' if the mean activity in area 9/46d in the last 500ms before the end of the trial was greater than 15Hz, and a 'Miss' otherwise. We trained each support vector classifier using scikit-learn in Python and standard parameter settings.[120] A separate classifier was trained for each timepoint in the training data. We then used each of these classifiers to predict the trial outcome based on activity at each time point in a separate test set. Finally, we compared these predictions to the actual trial outcome (defined according to the late sustained activity in 9/46d).

To estimate whether the coding pattern is similar between times t and t', we can train a classifier at time t (across trials) and test it at time t'. When applied across all pairs of timepoints, this leads to a square $T \times T$ temporal generalization matrix, where T is the number of timepoints.[17,43,44]

We assessed the strength of correlation between decoder coefficients (for the decoder trained at each timepoint) and the cortical hierarchy using Pearson correlations (Figure 3E). We conservatively judged the correlation at a particular timepoint to be significant only if the p value was less than 0.001 for all timepoints within a 10ms period centered on the timepoint.

Cell Reports, Volume *44*

Supplemental information

A dynamic bifurcation mechanism explains cortex-wide neural correlates of conscious access

Ulysse Klatzmann, Sean Froudist-Walsh, Daniel P. Bliss, Panagiota Theodoni, Jorge Mejías, Meiqi Niu, Lucija Rapan, Nicola Palomero-Gallagher, Claire Sergent, Stanislas Dehaene, and Xiao-Jing Wang

Supplemental Figures

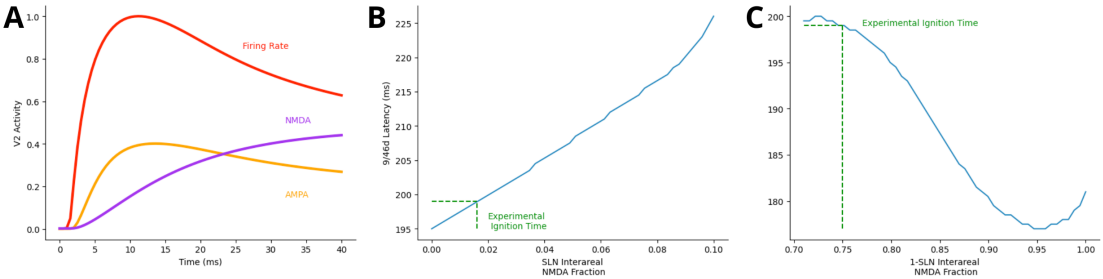

Supplemental Figure 1. Dynamics of AMPA and NMDA Receptor Activity and Their Impact on Ignition Timing Across Inter-Areal Connections *A) The dynamics of activity in area V2 (normalized firing rate) reflects the distinct dynamics of AMPA and NMDA receptors at feedforward and feedback connections. B) Impact of Receptor Type on Ignition Timing. Ignition times (time to reach 95% of peak dlPFC activity) vary with the fraction of NMDA receptors in inter-areal connections from B) SLN projections and C) 1-SLN projections.*

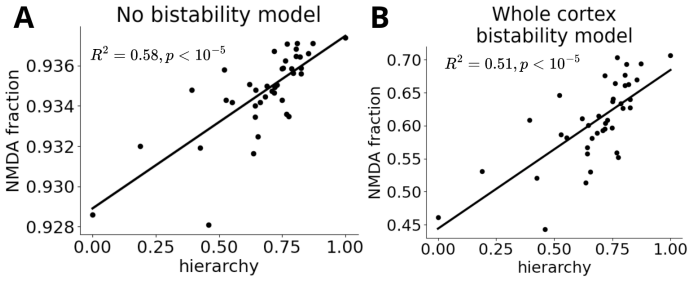

Supplemental Figure 2. NMDA Fraction Along the Cortical Hierarchy in Alternative Models *For both alternative models, the fraction of excitatory inputs via NMDA receptors (compared to total NMDA+AMPA inputs) increases along the cortical hierarchy.*

Supplemental Tables

Supplemental Table 1, Parameters for Numerical Simulations

Table S1. Parameters for Numerical Simulations

Parameter	Description	Value
τ^{NMDA}, τ^{AMPA}	E synaptic time constants	60ms,2ms
g^{NMDA}, g^{AMPA}	Channel Conductances	1000pA, 10000pA
τ^{GABA}	I synaptic time constant	5ms
τ^{R}	Firing rate time constant	2ms
γ_{NMDA}, γ_{AMPA}, γ_I	Synaptic rise constants	1.282, 2, 2
κ^{sup}, κ^{dp}, κ^{local}	NMDA fraction	0., 0.8, 0.91
ρ^{sup}, ρ^{dp}	Long-range E/I targets	1., 0.015
z^{min}	Min excitation value	0.6
z_I^{min}	Min excitation value	0.218
σ_{noise}	std. dev. of noise	2.5pA
I_E^{bg}, I_I^{bg}	Background inputs	329.4pA, 260pA
a, b, d	f-I curve (E cells)	0.135 Hz/pA, 54Hz, 0.308s
β_i, I_{th}	f-I curve (I cells)	153,75Hz/nA, 252Hz
b_1	Rescale FLN	0.3
$G_{E,E}^{N,loc}$	Excitatory NMDA strengths	480pA
$G_{E,E}^{A,loc}$	Excitatory AMPA strengths	4800pA
$G_{I,E}^{N,loc}$	Excitatory NMDA strengths to the Inhib Unit	10pA
$g_{E,I}$, $g_{I,I}$	Inhibitory strengths	-8800pA, -120pA
G_E^{NDMDA}, G_I^{NMDA}	Long-range NMDA strength	1500pA, 10.5pA
G_E^{AMPA}, G_I^{AMPA}	Long-range AMPA strength	15000pA, 105pA
G_0	Local balanced coupling	215pA
I^{stim}	Stimulus strength	250pA

Please note that this is a current-based model, so all synaptic strengths area given in units of pA.

Supplemental Table S2, Incubation protocols

Table S2: Incubation protocols

Table S2	AMPA	NMDA
[^{3}H]-Ligand	AMPA (10 nM)	MK-801 (3.3 nM)
Displacer	quisqualate (10 µM)	MK-801 (100 µM)
Incubation buffer	50mM Tris-acetate (pH 7.2) + 100 mM KSCN*	50mM Tris-acetate (pH 7.2) + 50 µM glutamate + 30 µM glycine* + 50 µM spermidine*
Preincubation	3 x 10 min, 4°C	15 min, 4°C
Main incubation	45 min, 4°C	60 min, 22°C
Final rinsing	1. 4 x 4 sec, 4°C 2. 2 x 2sec in 100/2.5 acetone/glutaraldehyde, 4°C	1. 2 x 5 min, 4°C 2. rinse in distilled water, 22 °C

* substance only included in buffer for the main incubation